nature materials

ARTICLES

https://doi.org/10.1038/s41563-019-0566-2

The entry of nanoparticles into solid tumours

Shrey Sindhwani[1,12], Abdullah Muhammad Syed[1,12], Jessica Ngai[1,2,13], Benjamin R. Kingston[1,13], Laura Maiorino[3,4,13], Jeremy Rothschild[5], Presley MacMillan[6], Yuwei Zhang[6], Netra Unni Rajesh[7], Tran Hoang[1], Jamie L. Y. Wu[1], Stefan Wilhelm[8], Anton Zilman[1,5], Suresh Gadde[9], Andrew Sulaiman[9], Ben Ouyang[1], Zachary Lin[1], Lisheng Wang[9], Mikala Egeblad[3] and Warren C. W. Chan[1,2,6,10,11*]

The concept of nanoparticle transport through gaps between endothelial cells (inter-endothelial gaps) in the tumour blood vessel is a central paradigm in cancer nanomedicine. The size of these gaps was found to be up to 2,000 nm. This justified the development of nanoparticles to treat solid tumours as their size is small enough to extravasate and access the tumour microenvironment. Here we show that these inter-endothelial gaps are not responsible for the transport of nanoparticles into solid tumours. Instead, we found that up to 97% of nanoparticles enter tumours using an active process through endothelial cells. This result is derived from analysis of four different mouse models, three different types of human tumours, mathematical simulation and modelling, and two different types of imaging techniques. These results challenge our current rationale for developing cancer nanomedicine and suggest that understanding these active pathways will unlock strategies to enhance tumour accumulation.

The successful delivery of anticancer agents to solid tumours is critical to their success for treatment and diagnosis[1]. For engineered nanomaterials, the central dogma is that nanoparticles pass through gaps between endothelial cells (inter-endothelial gaps) in the tumour blood vessels, which are formed during angiogenesis[2–5]. These gaps were found to have a size range up to 2,000 nm (refs [3,5]). Engineers and scientists use this as a rationale to design particles smaller than this size, expecting them to passively enter tumours and accumulate in sufficient quantity[1,6]. This principle of nanoparticle delivery was established in 1986 when Jain and Maeda's groups independently demonstrated that proteins and dyes could accumulate in the VX2 carcinoma and sarcoma 180 ascites tumour models[7,8]. In 1998, Jain's group attributed this enhanced tumour accumulation of engineered materials to gaps between endothelial cells[3]. This was demonstrated by injecting different-sized liposomes into mouse tumour models to identify the size ranges for accumulation and by visualizing a few gaps using transmission electron microscopy (TEM). The reported existence of these large permeable gaps and the development of methods to synthesize and tune the size and shape of nanoparticles drove the field of cancer nanomedicine for three decades. However, after 30 years of limited clinical translation, the field is questioning these mechanisms again[1,9–17]. We explored the phenomenon of nanoparticle tumour permeability and questioned the mechanism of nanoparticle entry into solid tumours. Answering this question is important because this is the first tumour barrier for nanoparticles to overcome to gain access to the microenvironment for specific therapeutic action. Determining the dominant mechanism will guide the design of delivery carriers.

Results

Frequency of gaps in tumours does not account for nanoparticle tumour accumulation. The current paradigm is that leaky vessels have gaps that allow nanoparticles to enter tumours (Fig. 1a). We first investigated the frequency of these gaps along tumour vessels. Our first line of evidence came from TEM analysis because it has a resolution of <2 nm and can resolve breaks within the endothelial lining of blood vessels (Fig. 1a,b). We analysed the vasculature of the U87-MG glioblastoma xenograft model because it was used previously to establish gaps as a potential route for extravasation[2,3]. We inoculated CD1-nude mice with U87-MG glioblastoma cells and allowed them to grow for three weeks. We then fixed and resected tumours and used an ultramicrotome to make 90 nm slices and imaged them using TEM. We observed a total of 21 gaps across all the analysed vessels of U87-MG tumours (Supplementary Note 1 gives the dataset). We also examined different tumour models, which included slower growing syngeneic (4T1, breast cancer), genetically engineered (MMTV-PyMT, breast cancer) and patient-derived xenograft (PDX) breast cancer because of their relevance to human tumours (Fig. 1b). Gaps occurred at a very low frequency in all the tumour types (Supplementary Table 1). Overall, we analysed 313 blood vessels across all the tumour models and found 26 gaps (Supplementary Note 1). The total sum of vessel length analysed was 9.2 mm (along the major axis) and 23.6 mm (vessel perimeter) (Supplementary Table 2). This amounts to an overall average of 2.8 gaps mm^{-1} (with respect to the total major axis length) and 1.1 gaps mm^{-1} (with respect to the total vessel perimeter). The overall gap coverage was calculated to be 0.048% of the blood vessel surface area (Nanoparticle diffusion model section in Supplementary

[1]Institute of Biomaterials and Biomedical Engineering, University of Toronto, Toronto, Ontario, Canada. [2]Chemical Engineering and Applied Chemistry, University of Toronto, Toronto, Ontario, Canada. [3]Cold Spring Harbor Laboratory, Cold Spring Harbor, NY, USA. [4]Watson School of Biological Sciences, Cold Spring Harbor, NY, USA. [5]Department of Physics, University of Toronto, Toronto, Ontario, Canada. [6]Department of Chemistry, University of Toronto, Toronto, Ontario, Canada. [7]Division of Engineering Science, University of Toronto, Toronto, Ontario, Canada. [8]Stephenson School of Biomedical Engineering, University of Oklahoma, Norman, OK, USA. [9]Department of Biochemistry, Microbiology, and Immunology, University of Ottawa, Ottawa, Ontario, Canada. [10]Donnelly Center for Cellular and Biomolecular Research, University of Toronto, Toronto, Ontario, Canada. [11]Materials Science and Engineering, University of Toronto, Toronto, Ontario, Canada. [12]These authors contributed equally: Shrey Sindhwani, Abdullah Muhammad Syed. [13]These authors contributed equally: Jessica Ngai, Benjamin R. Kingston, Laura Maiorino. *e-mail: warren.chan@utoronto.ca

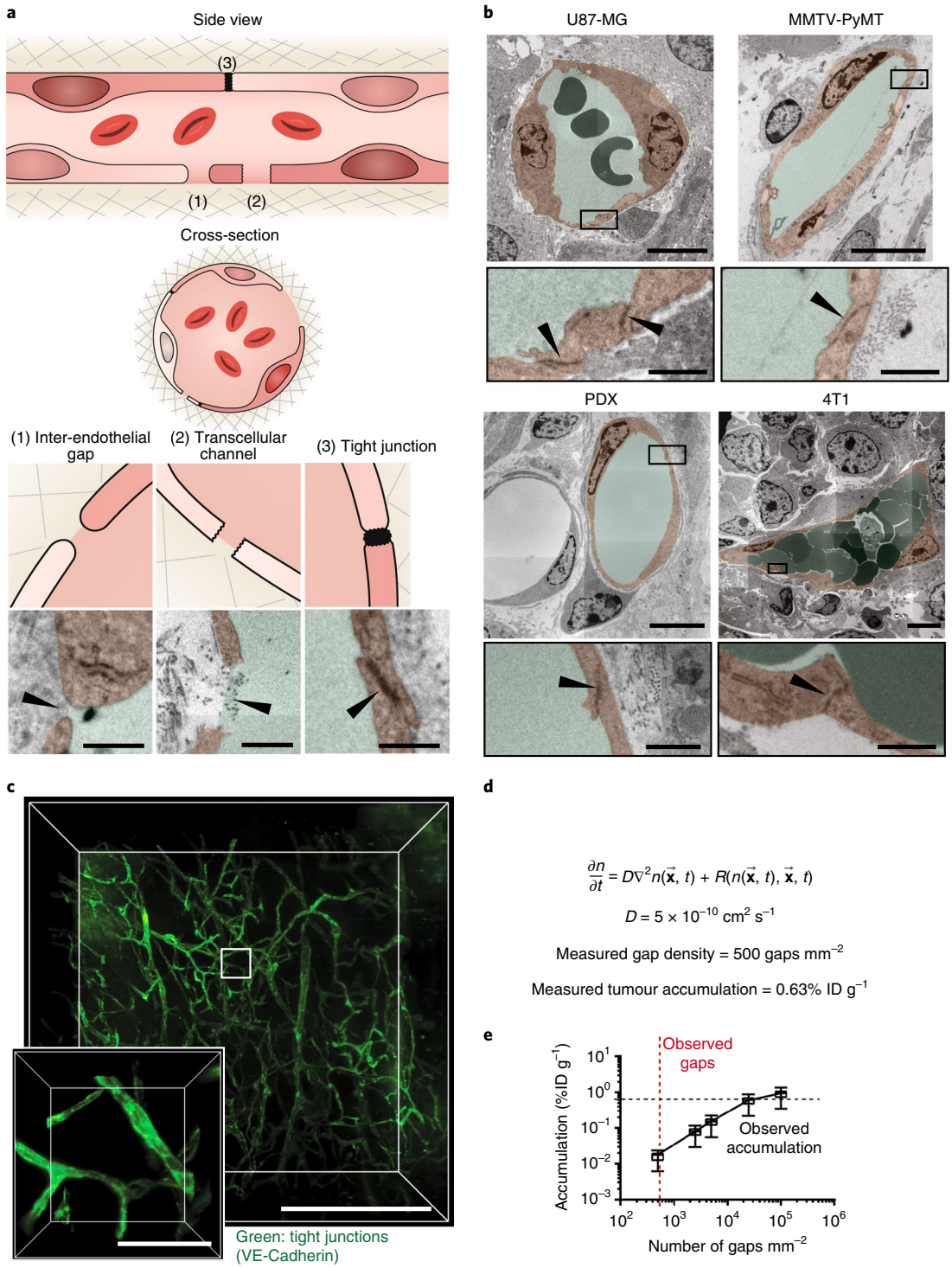

Fig. 1 | Tumour vasculature is mostly continuous and gaps occur at a very low frequency. a, Gaps along the endothelial lining can result from the breaking of tight junctions to form (1) inter-endothelial gaps or (2) transcellular channels. Both of these provide passive pathways for nanoparticle extravasation. Endothelial cells are connected to each other via (3) tight junctions. Corresponding TEM images below show these features along the blood vessel. Scale bars, (1) and (3), 500 nm; (2), 1 µm. **b**, Representative TEM images of tumour blood vessels across four different mouse tumour models show a continuous endothelial lining due to the intact tight junctions (filled arrows) with rare occurrences of gaps. Scale bars, 5 µm; insets, 1 µm. **c**, Representative large-volume 3D image of immunostained tight junctions (anti-VE-cadherin antibody, green) revealed continuous staining of the endothelium. Scale bars, 500 µm; inset, 100 µm. **d**, Equation and simulation parameters of the tumour accumulation of nanoparticles by varying the number of gaps, where $n(\mathbf{x},t)$ is the concentration of nanoparticles and $R(n(\mathbf{x},t)\mathbf{x},t)$ is a sink/source term. The observed tumour accumulation is 0.63% injected dose (ID) per gram of tumour. **e**, This requires a gap density of 20,000 gaps mm^{-2}. However, the measured gap density from TEM analysis is 500 gaps mm^{-2} (**d**). Gaps cannot explain the observed nanoparticle accumulation and distribution inside the tumour. The box–whisker plot is for $n = 12$ images in each condition (4 regions x 3 tumours). Centre line, median; box limits, upper and lower quartiles; whiskers, full range of values. Supplementary Table 10 gives the number of animals (n) for which the experiment was repeated.

Discussion). This corresponds to a gap density of 500 gaps mm^{-2} (see Supplementary Discussion for details). Surprisingly, only 7 out of 26 gaps were inter-endothelial, whereas the remaining 19 were transcellular channels. The current paradigm of nanoparticle transport into solid tumours is based on extravasating through inter-endothelial gaps to allow passive accumulation[2,3,5]. However, their extravasation through transcellular channels has not been explored. One way that these channels form is by the fusion of vesicles[18–24], which leads to the formation of a channel across the cell.

A limitation of the TEM analysis is that it surveys a small volume of the entire tumour. We addressed this issue by using three-dimensional (3D) microscopy as a second line of evidence (Fig. 1c)[25–27]. 3D microscopy enables us to qualitatively assess the vasculature in a continuous manner over large volumes and also avoids misinterpretations of gaps that might occur in 2D histology due to out-of-plane vessels. We perfused mice with fixative and cross-linkers, resected tumours and rendered them optically transparent for large volume 3D microscopy. Transparent tumours were then stained for tight junctions using antibodies against VE-cadherin (Fig. 1c). The blood vessels appeared to be uniformly stained and continuously labelled, which confirms the presence of intact tight junctions across large tumour volumes. The continuity of blood vessels is in line with the TEM analysis, which found gaps to be rare.

We next investigated whether the number of gaps observed via TEM is sufficient to explain the accumulation of nanoparticles in tumours. We did this by comparing the nanoparticle accumulation in tumours from two sources: mathematical modelling built using 3D images of tumour vasculature, and measuring the accumulation in tumours post-intravenous injection. This approach allowed us to determine if the accumulation in the tumour could be explained by the observed density of gaps. We developed a mathematical model of extravasation with varying numbers of gaps using the blood vessel networks mapped from 3D images of tumours (Methods and the Nanoparticle diffusion model section in Supplementary Discussion). We used the effective diffusion coefficient (D) previously determined by Jain and co-workers in the U87-MG model (Fig. 1d)[28]. We input the gap density based on our TEM observations (500 gaps mm^{-2}) and generated random gaps within 3D mapped vessels at this density. The map of vessels was derived from 3D images of U87-MG tumours. We compared the simulated nanoparticle accumulation against the measured accumulation using inductively coupled plasma–mass spectrometry (ICP-MS)[29]. We injected 50 nm PEGylated (PEG, polyethylene glycol) gold nanoparticles (AuNPs) (see Supplementary Table 3 for nanoparticle characterization) intravenously into tumour-bearing mice. The tumour was resected and digested to measure the AuNP accumulation using ICP-MS. We found that the simulated nanoparticle accumulation in the tumours was 0.0158% ID g^{-1}, which is 40-fold less than the ICP-MS measured accumulation of 0.63% ID g^{-1} (Fig. 1e). Our simulation shows that a gap density of ~30,000 gaps mm^{-2} would be required to explain the measured accumulation (Fig. 1e). The tumour has 60-fold fewer gaps than needed to explain the observed accumulation of nanoparticles. As our TEM analysis and simulation experiments show that tumour vessels are mostly continuous and do not have enough gaps to explain nanoparticle tumour accumulation, we investigated other mechanisms of nanoparticle extravasation.

Nanoparticles can enter tumours through trans-endothelial pathways. We next explored trans-endothelial pathways of nanoparticle extravasation. Schnitzer and co-workers previously showed that albumin binds to the gp60 protein in caveolae of endothelial cells for transport across the vasculature[11,30,31]. Dvorak and co-workers also showed that a subset of tumour and normal blood vessels form a chain of grape-like interconnected vesicles and vacuoles, termed vesiculo-vacuolar organelles, for transporting ultrasmall ferritin[1,18–22]. This transport pathway has relevance for transporting small-molecule drugs and albumin across tumour vasculature, but the role of tumour endothelial cells in transporting nanoparticles remains unexplored[18–20,23,24,30,32–34]. Transcytosis is a metabolically active process that requires endothelial cells to rearrange their cytoskeleton and cell membrane. This includes forming vesicles that can uptake nanoparticles, forming diaphragms called fenestrae or transporting through the cytoplasm (Fig. 2a)[18–20,23,24,30,32–34]. TEM analysis again formed our first line of evidence in looking at trans-endothelial transport because of the high resolution and compatibility with AuNPs (Fig. 2b,c). Our analysis of tumour vasculature across all the models found that fenestrae occur at an average frequency of 60 fenestrae mm^{-1} (with respect to the total major axis length) and 24 fenestrae mm^{-1} (with respect to the total vessel perimeter) (Supplementary Table 2). Vacuoles occurred at a frequency of 290 vacuoles mm^{-1} (with respect to the total major axis length) and 111 vacuoles mm^{-1} (with respect to the total vessel perimeter) (Supplementary Note 1). These structures occur much more frequently than the gaps. Next, we used TEM to investigate where the nanoparticles were along the blood vessel. AuNPs were injected intravenously into tumour-bearing mice and were circulated for different times (15 and 60 minutes). We then fixed tumours through cardiac perfusion with fixative. Thin sections were imaged and analysed by counting the nanoparticles and their associated vessel structures during extravasation. Each of the 289 vessels and 57,080 nanoparticles (Supplementary Table 4 and Supplementary Note 1) were analysed independently by 3 researchers to avoid bias and ensure internal validity. Annotated images were counted using MATLAB (MathWorks) to avoid any counting errors and bias. We found that nanoparticles interact with and are taken up by endothelial cells that lined tumour vessels (Fig. 2b,c and Supplementary Table 3). AuNPs of all three core sizes (15, 50 and 100 nm) were found inside the vesicles and cytoplasm and along the membrane of the endothelial cells of tumour vessels (Fig. 2b,c and Supplementary Tables 3 and 4). This is direct evidence that nanoparticles can use trans-endothelial pathways to extravasate into the tumour. This process is continuous as AuNPs were found to be extravasating at four hours (Supplementary Fig. 1). We quantified this transport by measuring the proportion of 50 nm AuNPs that extravasated between 15 and 60 minutes of circulation (Supplementary Table 5). The proportion of nanoparticles in the extravascular space of U87-MG and MMTV-PyMT tumours increased from 26–33% to 42–44% of the total quantified nanoparticles. Similar to mapping tight junctions, we used 3D microscopy as a second line of evidence to map the location of structures involved in the trans-endothelial pathway. PV-1 is a structural protein found in fenestrae and vesicles[35–37]. We stained our transparent tumours with antibodies against PV-1 and found continuous labelling of endothelial cells (Fig. 2d). This uniform labelling is also in line with our TEM analysis of fenestrae and vesicles which occurred at a very high frequency along the blood vessels. Our analysis yields two conclusions. First, gaps occur infrequently along tumour vessels. Second, nanoparticles can use active transport through trans-endothelial pathways to enter solid tumours. This made us question which mechanism among these two mechanisms—passive transport through gaps or active transport through trans-endothelial pathways—accounts for the majority of nanoparticle accumulation in tumours.

Trans-endothelial pathways are the dominant mechanism of nanoparticle extravasation into tumours. We do not know which of the above mechanisms dominates because it remains elusive to isolate and measure their individual contributions to nanoparticle accumulation in tumours. We solved this challenge by developing a model, termed Zombie, in which tumour-bearing mice were perfused with a fixative to deactivate any cellular activity while preserving the vessel architecture (Fig. 3a,b and Supplementary Video 1).

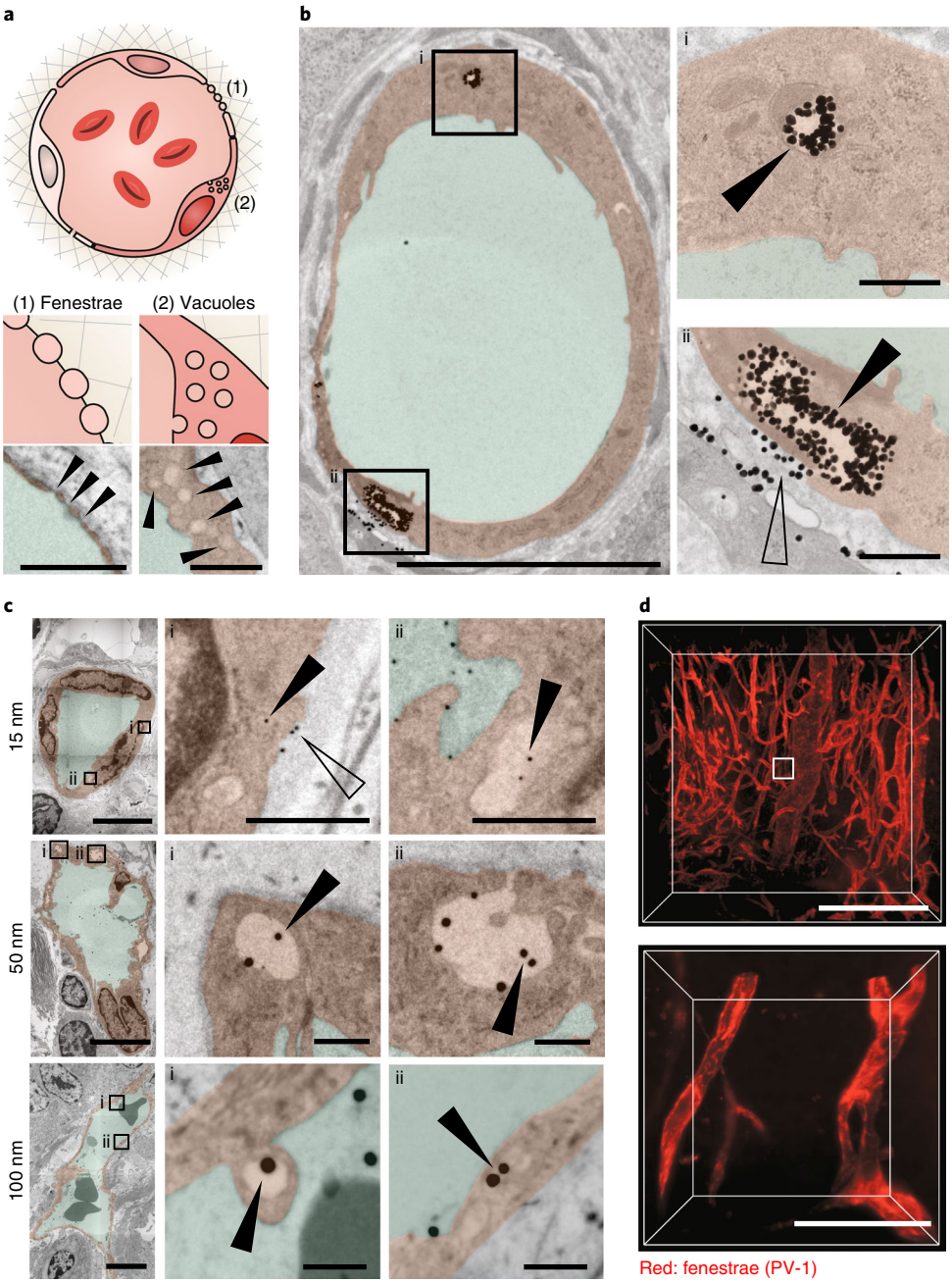

Fig. 2 | Nanoparticles can extravasate through active trans-endothelial pathways. a, Trans-endothelial pathways for nanoparticles include (1) formation of fenestrae and (2) uptake in vesicles and cytoplasmic shuttling. The corresponding TEM images show these features along the blood vessel. Scale bars, 500 nm. **b**, Nanoparticles were found inside the vesicles of the endothelial cells (filled arrows), which confirms their uptake and subsequent extravasation (open arrows) through a trans-endothelial pathway. Scale bars, 5 µm; insets, 500 nm. **c**, Nanoparticles of all three different core sizes (15, 50 and 100 nm) found inside the cytoplasm and vesicles of endothelial cells (filled arrows). Endothelial cells were also found to be emptying the nanoparticles into the tumour (open arrow). Scale bars, 5 µm; insets, 500 nm. **d**, Representative large-volume 3D image of immunostained vesicles and fenestrae (anti-PV-1 antibody, red) revealed continuous staining of the endothelium. Scale bars, 500 µm; inset, 100 µm. Supplementary Table 2 gives the number of animals for which the experiment was repeated in the animals and vessels columns.

This model allowed us to separate the contribution of passive gap and active trans-endothelial transport and determine the dominant mechanism because the active mechanisms are deactivated. We hypothesized that the fixation step in the Zombie model would block the morphological changes that underlie trans-endothelial transport but would keep gaps along the tumour vessels open for nanoparticle extravasation. We validated this by showing that: (1) no new gaps were created in tissues such as muscle and skin (Fig. 3c,d), (2) kidney gaps maintained their size (~6.5 nm) as they did not allow 50 nm AuNPs to pass through (Fig. 3e) and (3) gaps in liver sinusoidal endothelial cells remained open for nanoparticle accumulation (Fig. 3f). We provide a detailed validation of the Zombie model in the Supplementary Discussion. As AuNPs can be quantified using ICP-MS and imaged with 3D microscopy[25–27,38], we compared nanoparticle accumulation in Zombie and tumour-bearing live mice (that is, control tumours) to delineate the individual contributions of passive gaps and active trans-endothelial mechanisms (Fig. 3a).

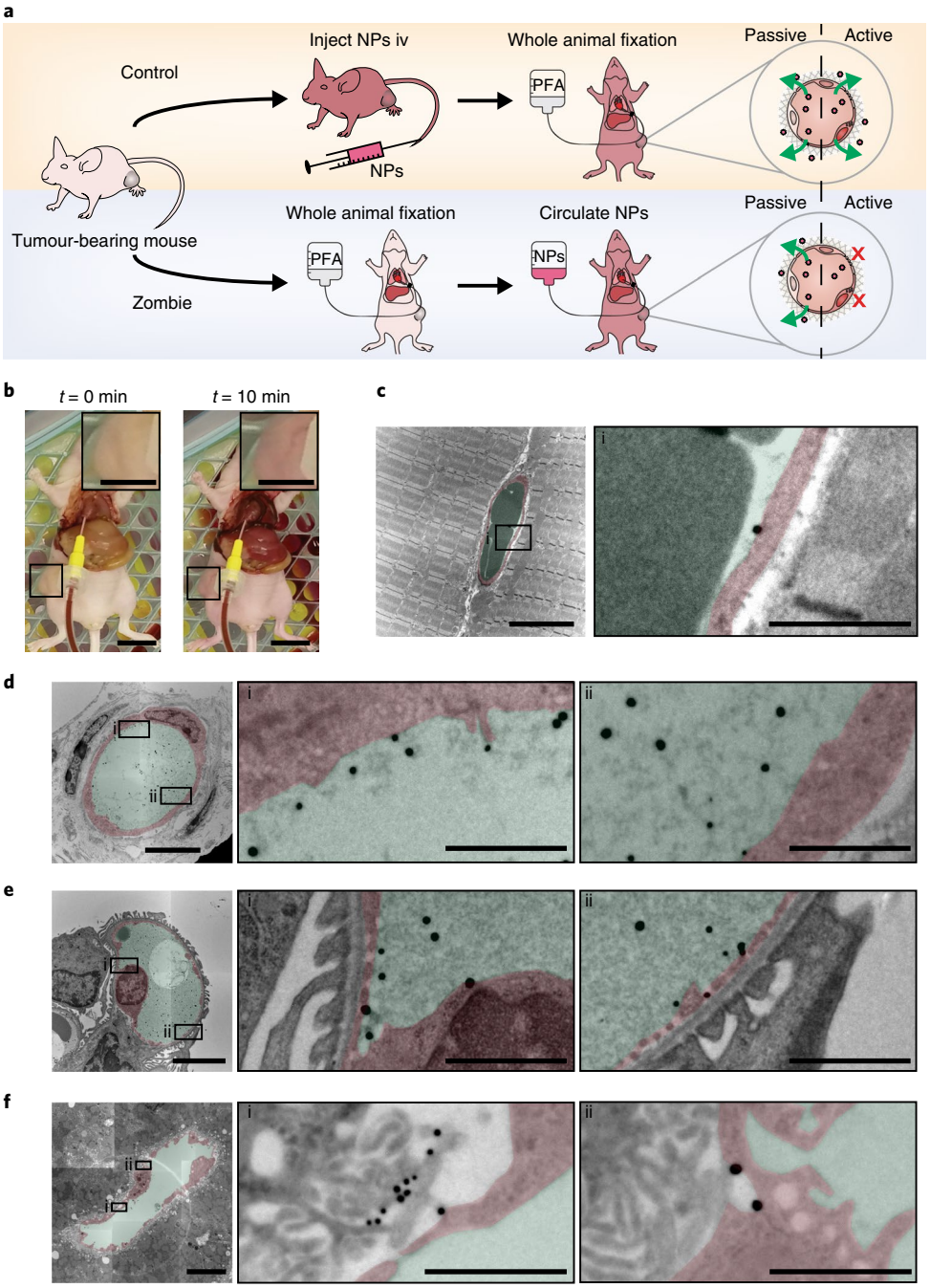

Fig. 3 | Zombie model preserves the architecture of vessels inside the animal. a, To isolate the role of passive pathways for nanoparticle extravasation, we developed a mouse model termed Zombie, whereby the mouse is first fixed and then circulated with nanoparticles. The accumulation in this model is due to only passive pathways, such as gaps, compared to control mice, which account for both gaps and trans-endothelial pathways. This allows for the isolation of the contribution of each of those pathways. **b**, Photographs of mice before and after perfusion of the nanoparticles through cardiac access. Before the nanoparticles were injected, the mouse was fixed and appears white because of the lack of blood. Within 10 min of nanoparticle perfusion, organs turn red as the nanoparticles circulate through the preserved vasculature. Scale bars, 2 cm; insets, 1 cm. **c**–**f**, TEM images of various tissues from the Zombie model show that the vessel architecture is preserved. Vessels of the muscle (**c**) and skin (**d**) remain continuous and the nanoparticles remain localized to the lumen. There is no extravasation. The kidney (**e**) and liver (**f**) are examples of tissues that have gaps to allow for filtration. The 50 nm AuNPs cannot cross the kidney glomerular filtration unit because their size is above the ~6 nm cutoff. The sinusoidal endothelial cell lining of liver vessels has bigger gaps and allows for nanoparticle extravasation into the space of Disse. These examples of positive and negative controls validate that the Zombie model preserves the architecture of blood vessels and their ability to filter nanoparticles. Scale bars, 5 μm; insets, 1 μm. Supplementary Table 10 gives the number of animals (*n*) for which the experiment was repeated. NPs, nanoparticles; PFA, paraformaldehyde.

We used the Zombie model to determine the dominant mechanism of nanoparticle accumulation. We obtained three measurements of nanoparticle accumulation: by ICP-MS, by TEM and by 3D microscopy in optically transparent cleared tumours. First, we quantified the nanoparticle tumour accumulation in Zombie and control tumour-bearing mice using ICP-MS. AuNPs of three different

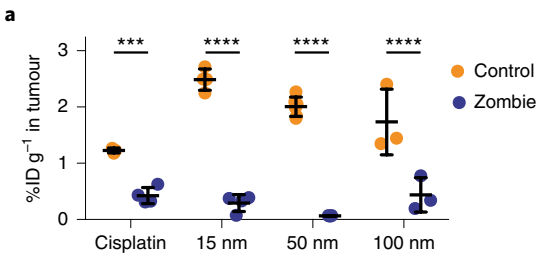

b

NP type	% attributed to gaps
Cisplatin	35
15 nm	12
50 nm	3
100 nm	25

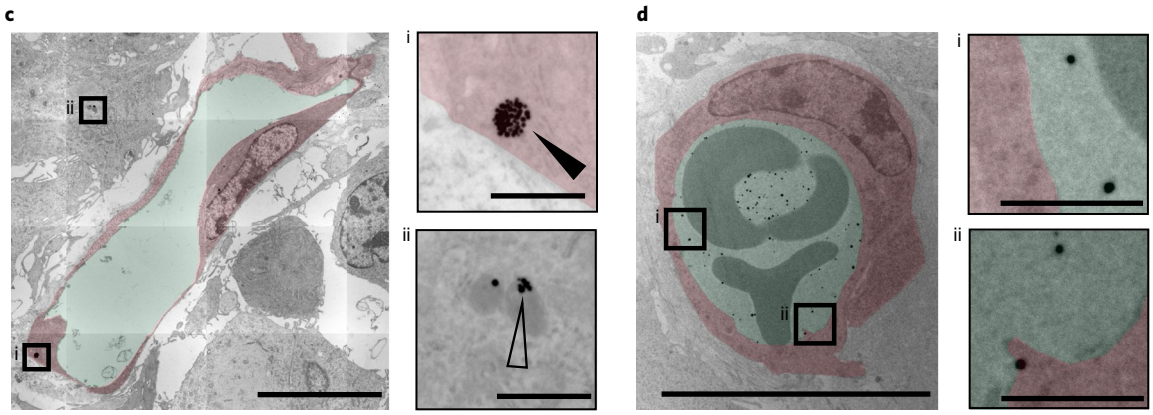

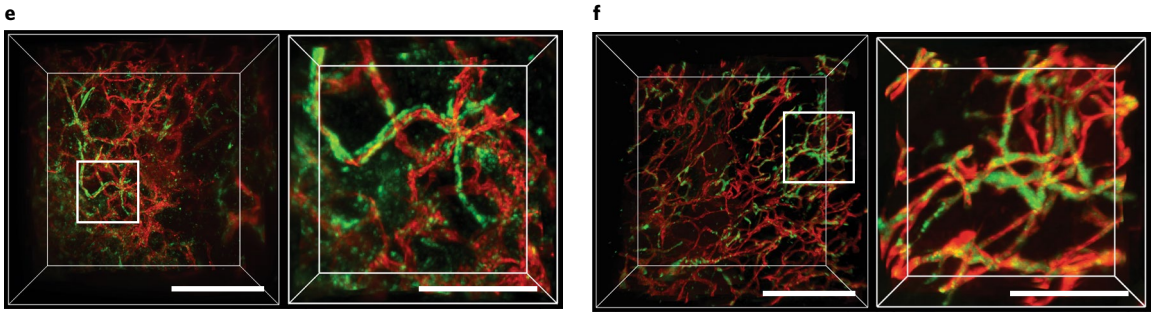

Blood vessels (GSL-1-Cy3), nanoparticles (darkfield)

g

Model	Lumen (%)	Side wall (%)	Vacuole (%)	Cytoplasm (%)	Extravascular (%)	No. of vessels	Length (μm)	Total no. of NPs
Control	25.9 ± 26.2	2.7 ± 3.6	10.8 ± 12.2	11.8 ± 18.7	48.8 ± 25.8	22	596	2,281
Zombie	84.5 ± 14.1	15.1 ± 13.6	0.0 ± 0.0	0.4 ± 0.6	0.0 ± 0.0	20	333	2,372

Fig. 4 | The dominant mechanism of nanoparticle entry into solid tumours is trans-endothelial. a, ICP-MS quantification of gold and the platinum content (from cisplatin) in tumours collected from Zombie and control animals shows that passive pathways account for the minority of nanoparticle accumulation in the tumour (Supplementary Tables 10 and 11 give *n*, degrees of freedom and *F* value). ***$P < 0.001$, ****$P < 0.0001$. Plots indicate the mean and s.d. **b**, Dividing the nanoparticle accumulation in tumours from Zombie mice by that from the control provides the contribution of the passive pathways, such as gaps. **c**,**d**, TEM shows that the nanoparticles remained within the lumen in Zombie tumours with the architecture remaining preserved (**d**). In control animals (**c**), the nanoparticles were taken up into the endothelial cells and extravasated into the perivascular tumour matrix. Filled arrows show nanoparticles in a vacuole within an endothelial cell. The open arrow shows nanoparticles within the tumour. Scale bars, 10 μm; insets, 1 μm. **e**,**f**, 3D microscopy of these tumours show that nanoparticles (green) remain localized in the Zombie tumour vessels (red) (**f**), whereas they were able to extravasate in the control mice (**e**). Scale bars, 500 μm; insets, 200 μm. **g**, Nanoparticles were able to extravasate out of control animals because their active pathways were intact. Zombie animals showed minimal nanoparticle extravasation out of tumours (reported values in the table are mean and s.d.).

sizes (15, 50 and 100 nm) and cisplatin (as a small-molecule drug control) were circulated inside both Zombie and control tumour-bearing mice. After circulating the nanoparticles for the same amount of time and the same concentration inside the animal, tumours were resected and digested to measure the amount of gold using ICP-MS. This measurement gave us the relative amount of injected dose (ID) of nanoparticles that accumulated in the tumour (Supplementary Table 6). We found that tumours in Zombie mice only accumulated 0.10% ID g^{-1} of the 50 nm AuNP dose, whereas control mice accumulated 2.01% ID g^{-1} after four hours (Fig. 4a). As Zombie mice do not have a functional clearance system to cause the exponential decay of nanoparticle concentration in blood, we corrected for it in the Zombie tumours by adjusting the accumulation based on the observed area under the curve of nanoparticles in blood in the control (see Methods for a detailed explanation). We found that the relative contribution of gaps for 50 nm AuNP is only 3% compared to that of the control. We repeated this experiment in a genetically engineered MMTV-PyMT tumour model that

mimics human breast cancer. We found a similar relative contribution of gaps (Supplementary Table 6 and Supplementary Fig. 2). We also repeated the experiment with the inclusion of red blood cells in addition to nanoparticles and serum in the circulation and found similar relative contribution of gaps (Supplementary Fig. 3). We found that the contribution of gaps to drug accumulation is size dependent: it ranged from 35% for cisplatin (M_r, 300 Da) to 3% for 50 nm AuNPs (Fig. 4b). Surprisingly, we found the relative contribution increased to 25% for 100 nm AuNPs (Fig. 4b). The contribution of different trans-endothelial transport pathways may vary with size and requires further investigation. Overall, gaps only account for 3–25% of the nanoparticle extravasation. We further imaged tumours in Zombie and control mice using TEM and 3D microscopy to investigate whether nanoparticles were able to extravasate out of vessels and into the tumour microenvironment (Fig. 4c–f). We found that nanoparticles were able to extravasate in control animals but not in Zombie animals. We quantified this from TEM images to find that 49% of the AuNPs had extravasated in control animals compared to 0% in Zombie mice (Fig. 4g). 3D microscopy also showed that AuNPs remained localized within the blood vessels of Zombie mice, but were able to extravasate deeper into the tumour in control mice (Fig. 4e,f). We attribute these spatial findings to trans-endothelial pathways being active in control animals. Our quantitative and imaging data show that the dominant mechanism for nanoparticle entry is trans-endothelial.

Our fourth line of evidence came from evaluating the endothelial features that are closest to the extravasated nanoparticles. We tested for correlations between the location of extravasated nanoparticles with active trans-endothelial or passive gap-based transport pathways. For each image of a blood vessel, we divided the vessel into ten bins along the circumference of the blood vessel (Fig. 5a,b). We measured the number of extravasated nanoparticles and blood vessel features (tight junctions, fenestrae, vesicle and inter-endothelial gaps and transcellular channels) within each bin (Supplementary Note 2 gives the key). We counted nanoparticles that touched the luminal wall of the endothelial cell, and that were inside endothelial vesicles and cytoplasm. For all the images, we performed correlative analysis between the extravasated nanoparticles, blood vessel features and nanoparticles associated with endothelial cells (Fig. 5a). The correlation between extravasated AuNPs and endothelial features is strongest with tight junctions (P value of 4.28×10^{-13}), even though these junctions form a seal that prevents nanoparticle transport (Fig. 5b). The region close to the tight junction is the thinnest part of the lumen, which may allow transport through invaginations that form vesicles and fenestrae[21,22,24]. Extravasated AuNPs also significantly correlated with vesicles (P value of 6.44×10^{-7}) (Fig. 5b) and with nanoparticles found in one of the intermediary states of trans-endothelial transport (P values: nanoparticle on the luminal wall, 1.00×10^{-6}; nanoparticle in an endothelial cell vesicle, 2.86×10^{-6}, nanoparticle in the endothelial cell cytoplasm, 8.07×10^{-10}) (Fig. 5b). This suggests that extravasated nanoparticles most likely followed one of these routes as they entered the tumour microenvironment. Our spatial analysis also shows that nanoparticle extravasation did not correlate significantly with any type of gaps, which is the basis for the current dogma of nanoparticle extravasation into tumours (P values: intercellular gaps, 0.54; transcellular channels, 0.097; all gaps, 0.14). Surprisingly, when gaps were found, nanoparticles were not found near most of them (Supplementary Fig. 4). Our spatial analysis also supports the trans-endothelial route as the dominant pathway of nanoparticle extravasation into the tumour (Supplementary Fig. 5 gives the methodology).

Last, we performed intravital microscopy to look at nanoparticle extravasation in two mouse tumour models (Fig. 5c,d). Intravital microscopy captures the dynamic aspect of nanoparticle extravasation, which is different from static techniques used above. This enabled us to image the nanoparticle extravasation in real time and monitor their signal colocalization with other elements of the microenvironment. We saw focal spots of colocalization between the nanoparticle signal and endothelial cells (Fig. 5c,d and Supplementary Video 2). These areas of nanoparticle colocalized with blood vessels indicate interactions between the nanoparticles and endothelial cells. These spots are not transient. We attribute these spots to different stages of extravasation via transcytosis that occurs in the endothelial cell vicinity, such as uptake, vesicular localization and exit into the tumour interstitium, as seen with TEM (Supplementary Fig. 1).

The combination of these five lines of evidence reinforces the conclusion that nanoparticles enter the tumour from blood vessels predominantly due to active trans-endothelial mechanisms. We attempted to find if one of the known pathways could be involved in transcytosis of the nanoparticles across the tumour endothelium. Based on work by other labs[39–43], we investigated the role of caveolin and vessel normalization on nanoparticle transport and tumour accumulation. We found that the tumour accumulation of 50 nm AuNPs did not change by either knocking out caveolin-1 (Supplementary Figs. 6–8 and Role of caveolin-1 section in Supplementary Discussion) or by vessel normalization through VEGFR-2 blockade using DC101 (Supplementary Fig. 9 and Role of vessel normalization section in Supplementary Discussion). Future work that investigates these pathways for different nanoparticle types and chemistries, as well as tumours, will allow us to evaluate their broader role in extravasation.

Gaps are also rare in tumour vessels from cancer patients. We wanted to ensure that the discovery of nanoparticle trans-endothelial transport was generalizable and relevant for tumours in humans. We found evidence for trans-endothelial transport of nanoparticles in xenograft (U87-MG), syngeneic (4T1, breast cancer), genetically engineered (MMTV-PyMT, breast cancer) and PDX breast cancer mouse models (Supplementary Table 7). We also examined human patient tumour samples to compare blood vessel structures with mouse models results (Fig. 6 and Supplementary Table 8). We obtained fixed human tumour samples that belong to three different tumours types from the Ontario Tumour Bank. These tissues were then fixed and sliced for TEM and 3D microscopy to investigate the vessel ultrastructure and analyse the large-volume tumour, respectively. We found that the blood vessels in human tumours were similar to those in mouse models. Specifically, we found that the frequency of features was similar to that in mouse models as shown in Supplementary Table 1 and that human tumours also had sealed blood vessels with tight junctions and fenestrae along the endothelial lining (Fig. 6 and Supplementary Table 8). The features were structurally identical when compared at an ultrastructure level across different human tumour models and with mouse models. Similar to 3D microscopy for mouse models, we immunolabelled tight junctions (VE-cadherin) and a component of diaphragms of fenestrae and vesicles (PV-1) in human samples. The vessels stained uniformly with these markers in large volumes, which indicates that the vessels are sealed and that they express proteins associated with transcytosis (Fig. 6d–f and Supplementary Video 3). Magnified images show clear patterns of junctional staining that mark the endothelial walls with no discontinuity (Fig. 6d–f). This is similar to our findings in mice models. The combined evidence from TEM and 3D microscopy shows that opportunities for cancer nanomedicine to enter tumours passively are also rare in human tumours because there are not enough gaps.

Discussion

We investigated whether nanoparticles are being transported into the tumour microenvironment by a passive or active process. Many perspectives have been written on this topic but there is a lack of original data that enables researchers to address this question[1,13].

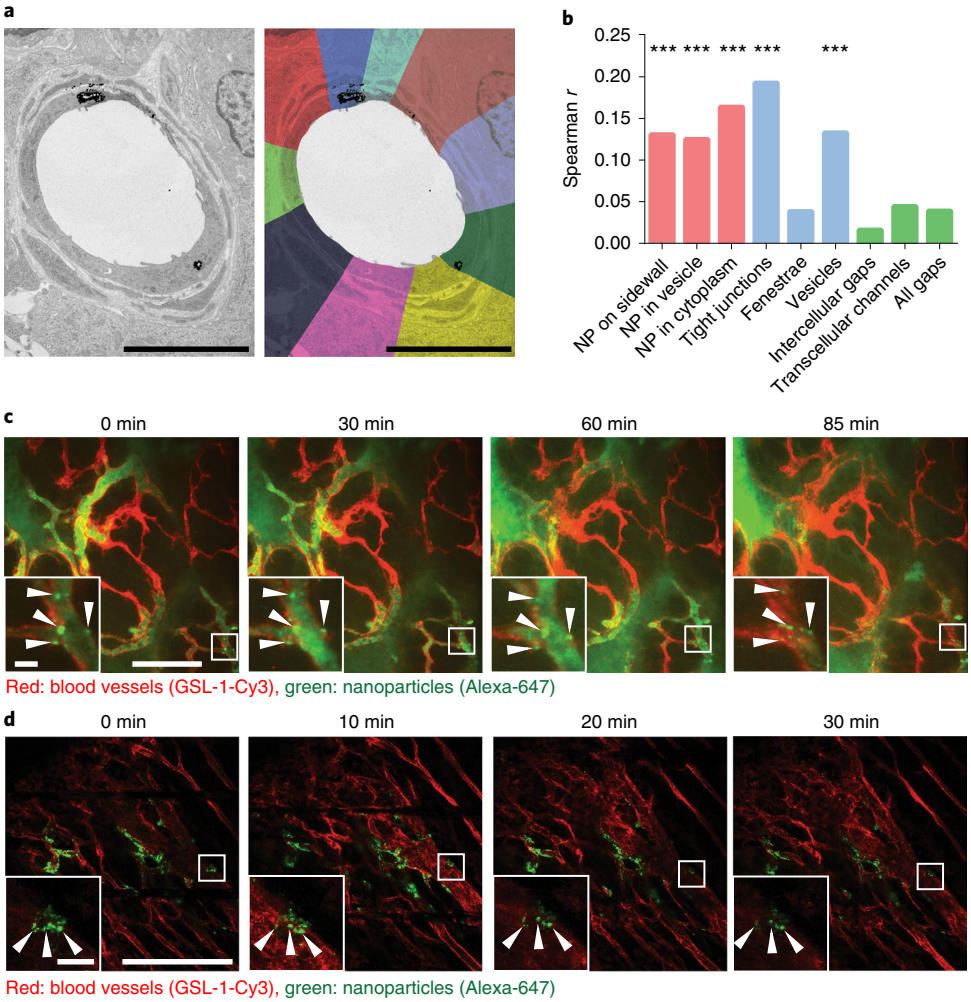

Fig. 5 | Nanoparticles correlate significantly with trans-endothelial pathways of transport. a, The blood vessel TEM image is divided into bins and extravasated nanoparticles and selected blood vessel features are counted in each bin. Scale bars, 5 µm. **b**, Analysis of all the extravasated nanoparticles with respect to the vessel features and nanoparticles within the lumen and endothelial cells. Spearman correlation coefficients are shown with two-tailed significance testing in all cases. Extravasated nanoparticles correlated significantly with the trans-endothelial features, such as vesicles and cytoplasm (red). *P* values: nanoparticle (NP) sidewall, 1.00×10^{-6}; NP vesicle, 2.86×10^{-6}; NP cytoplasm, 8.07×10^{-10}. They also correlated significantly with nanoparticles touching the side wall, inside the vesicles and inside the cytoplasm (blue). *P* values: tight junction, 4.28×10^{-13}; fenestrae, 0.15; vesicles, 6.44×10^{-7}. Thus, a nanoparticle that had just extravasated also correlated with the intermediary steps of extravasation starting in the same region, such as cell–wall interaction and being taken up into vesicles and cytoplasm. Extravasated nanoparticles did not correlate with gaps (green). *P* values: intercellular gaps, 0.54; transcellular channels, 0.097; all gaps, 0.14. $^{***}P<10^{-6}$. **c**,**d**, Intravital imaging shows colocalization of the nanoparticles with endothelial cells to form hotspots along the vessel lining (red, stained with GSL1-Cy3). Arrows indicate hotspots. These vessels belong to the MMTV-PyMT (**c**) and 4T1 (**d**) tumour models. The 50 nm AuNPs (green) were conjugated with Alexa Fluor 647 for the fluorescent signal. Scale bars, 200 µm; insets, 20 µm. For **b**, 126 vessels were analysed (all the vessels that contained extravascular nanoparticles at 0.25 h postinjection). Significance was determined using a two-tailed bivariate Spearman ρ analysis. *P* values were adjusted using the Bonferroni correction for multiple comparisons. For **c** and **d**, the images are representative of three biologically independent mice for each tumour type.

The lack of data is likely due to multiple reasons. First, there is the lack of a single technique capable of visualizing individual nanoparticles entering into solid tumours. Second, there is a lack of studies that directly examine this mechanism. All the techniques used have advantages and disadvantages in addressing this question and, thus, answering it requires a multitude of complementary techniques. For example, TEM has nanoscale resolution but is static and has a limited volume of analysis. Intravital microscopy can provide real-time analysis of nanoparticle transport into tumours, but the resolution is limited[44]. Thus, we gathered multiple lines of evidence from different techniques and models to answer how nanoparticles enter solid tumours.

We examined the current paradigm that nanoparticles are transported through gaps measuring up to 2,000 nm between endothelial cells in a tumour[3,5,7,44]. This mechanism suggested that researchers should design particles smaller than this size to enter the tumour. We found that gaps occurred rarely and that transport through them was not the dominant mechanism of entry into mouse tumour models using a combination of TEM, 3D imaging, the Zombie experiment and computational analysis. We analysed over 300 randomly selected vessels because our computational analysis revealed that this large number of vessels is required to reduce the probability of measuring anomalies in the tumour gap frequency due to random angle sectioning of the tissue sample (Sampling section in Supplementary Discussion). The sample preparation itself was randomized and blinded as well. These observations were further tested by the Zombie model, which decoupled the contribution of passive and active mechanisms. We corroborated these results

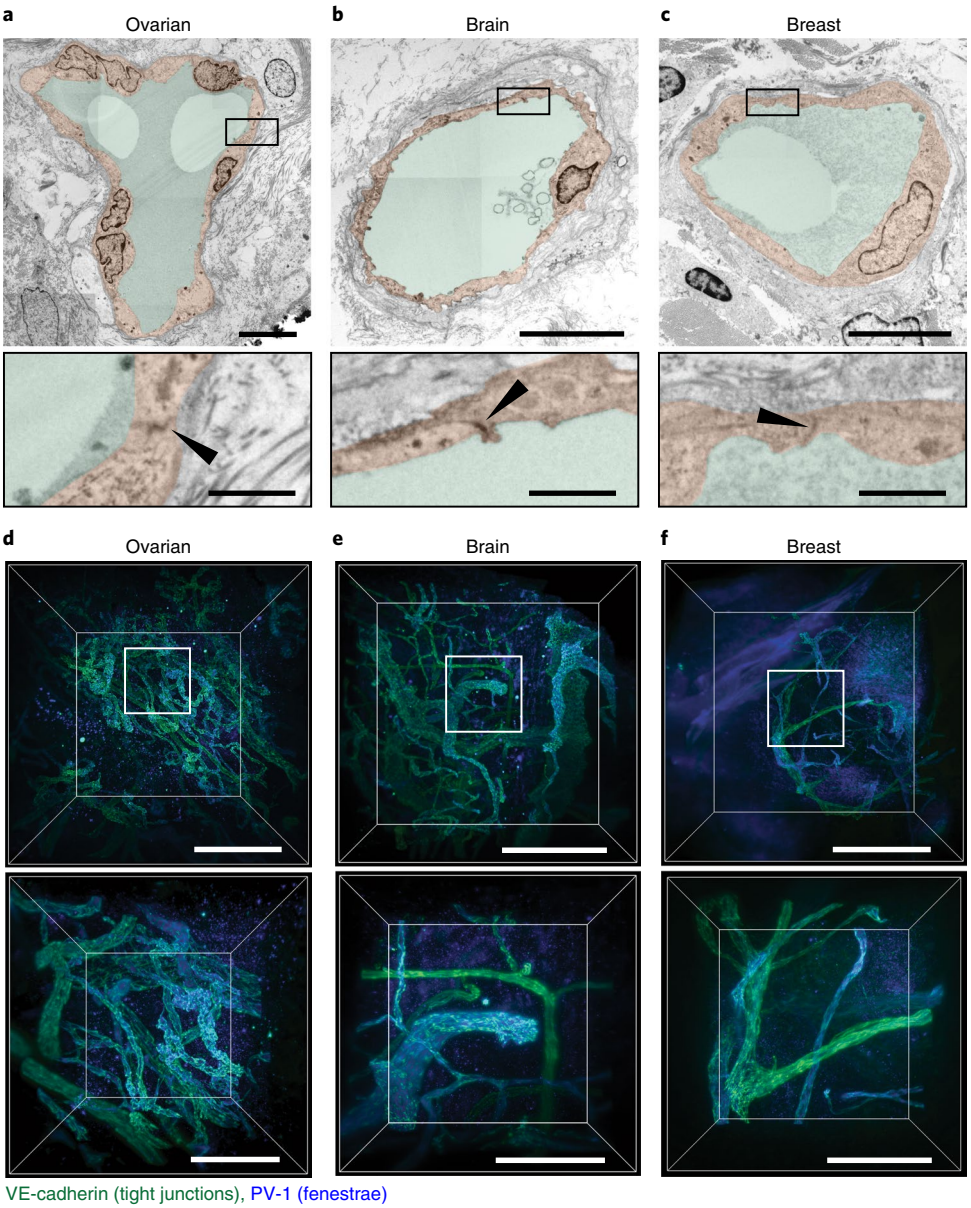

Fig. 6 | Tumour vessels in cancer patients are continuous with similar structural features to those of mouse models. a–c, Ultrastructure TEM imaging and analysis of tumour vessels from patient biopsies showed that vessels are sealed and continuous across different tumour types (ovarian, breast and glioblastoma). Arrows indicate tight junctions. Gaps were found very rarely. Scale bars, 5 µm; insets, 1 µm. **d–f**, 3D microscopy of these patient samples with VE-cadherin (green) shows the uniform presence of tight junctions along the vessels over large volumes. Anti-PV-1 staining (blue) shows blood vessels and specifically stains for PV-1 protein found in fenestrae and vesicles along the blood vessels. Scale bars, 500 µm; insets, 200 µm. Images are representative from three biologically independent tumours per tumour type. For each tumour patient sample, 7–10 tissue slices were visualized using TEM.

by simulating nanoparticle extravasation through gaps in our 3D images and found that the observed gap frequency from TEM could not account for the measured nanoparticle tumour accumulation. We consistently found that passive extravasation contributed only a fraction of the nanoparticle tumour accumulation.

This motivated us to look for an alternative transport mechanism. We again used a combination of tools, such as TEM, intravital imaging and 3D imaging across multiple tumour models to look for nanoparticles extravasating actively through endothelial cells. An active process could occur in many forms. This could be due to the binding of nanoparticles to endothelial cells and transport through them inside vesicles, transport through transcellular channels that are formed through connecting vesicles and/or fenestrae or any other mechanisms that have not yet been discovered. All these processes are dynamic, require energy to drive the transport and can vary between tumours. The next set of studies (discussed below) should delve deeper into these mechanisms to establish a further understanding of how nanoparticles are actively transported through tumour endothelial cells.

Outlook

Our key finding is that the dominant mechanism of nanoparticle transport is an active process and not a passive process. This will probably lead to debates, discussion, and studies that should aim at refining and manipulating the specific active mechanisms of transport. We have placed the original data in the open source FigShare for access. We outline 5 areas of investigation moving forward. First, we need to identify molecular mechanisms that drive the trafficking

of nanoparticles into solid tumours. Second, we need to understand the role of surface adsorbed proteins on nanoparticle interaction with tumour endothelial cells. Third, we can devise strategies to manipulate tumour endothelium to enhance the trans-endothelial transport of nanoparticles (an example of this has been demonstrated by the Schnitzer lab for antibody transport[32]). Fourth, the role of different tumour vessel types and different trans-endothelial pathways with respect to extravasation of varying nanoparticle size, shape and surface chemistry needs to be elucidated. Lastly, we also need to understand the role of immune cells and other cells generating transient permeability[45,46]. These studies will fill remaining gaps in our understanding of nanoparticle entry into tumours and enable strategies to overcome the poor clinical translation of cancer nanomedicines.

Online content

Any methods, additional references, Nature Research reporting summaries, source data, extended data, supplementary information, acknowledgements, peer review information; details of author contributions and competing interests; and statements of data and code availability are available at https://doi.org/10.1038/s41563-019-0566-2.

Received: 16 February 2019; Accepted: 15 November 2019;
Published online: 13 January 2020

References

1. Wilhelm, S. et al. Analysis of nanoparticle delivery to tumours. *Nat. Rev. Mater.* **1**, 16014 (2016).
2. Jain, R. K. Transport of molecules, particles, and cells in solid tumors. *Annu. Rev. Biomed. Eng.* **1**, 241–263 (1999).
3. Hobbs, S. K. et al. Regulation of transport pathways in tumor vessels: role of tumor type and microenvironment. *Proc. Natl Acad. Sci. USA* **95**, 4607–4612 (1998).
4. Jain, R. K. & Stylianopoulos, T. Delivering nanomedicine to solid tumors. *Nat. Rev. Clin. Oncol.* **7**, 653–664 (2010).
5. Hashizume, H. et al. Openings between defective endothelial cells explain tumor vessel leakiness. *Am. J. Pathol.* **156**, 1363–1380 (2000).
6. Peer, D. et al. Nanocarriers as an emerging platform for cancer therapy. *Nat. Nanotechnol.* **2**, 751–760 (2007).
7. Gerlowski, L. E. & Jain, R. K. Microvascular permeability of normal and neoplastic tissues. *Microvasc. Res.* **31**, 288–305 (1986).
8. Matsumura, Y. & Maeda, H. A new concept for macromolecular therapeutics in cancer chemotherapy: mechanism of tumoritropic accumulation of proteins and the antitumor agent smancs. *Cancer Res.* **46**, 6387–6392 (1986).
9. Nichols, J. W. & Bae, Y. H. EPR: evidence and fallacy. *J. Control. Release* **190**, 451–464 (2014).
10. Danhier, F. To exploit the tumor microenvironment: since the EPR effect fails in the clinic, what is the future of nanomedicine? *J. Control. Release* **244**, 108–121 (2016).
11. Kim, S. M., Faix, P. H. & Schnitzer, J. E. Overcoming key biological barriers to cancer drug delivery and efficacy. *J. Control. Release* **267**, 15–30 (2017).
12. Nakamura, Y., Mochida, A., Choyke, P. L. & Kobayashi, H. Nanodrug delivery: is the enhanced permeability and retention effect sufficient for curing cancer? *Bioconjug. Chem.* **27**, 2225–2238 (2016).
13. Nel, A., Ruoslahti, E. & Meng, H. New insights into 'permeability' as in the enhanced permeability and retention effect of cancer nanotherapeutics. *ACS Nano* **11**, 9567–9569 (2017).
14. Huynh, E. & Zheng, G. Cancer nanomedicine: addressing the dark side of the enhanced permeability and retention effect. *Nanomedicine* **10**, 1993–1995 (2015).
15. Nakamura, H., Jun, F. & Maeda, H. Development of next-generation macromolecular drugs based on the EPR effect: challenges and pitfalls. *Expert Opin. Drug Deliv.* **12**, 53–64 (2015); erratum **12**, 691 (2015).
16. Rosenblum, D., Joshi, N., Tao, W., Karp, J. M. & Peer, D. Progress and challenges towards targeted delivery of cancer therapeutics. *Nat. Commun.* **9**, 1410 (2018).
17. Chan, W. C. W. Nanomedicine 2.0. *Acc. Chem. Res.* **50**, 627–632 (2017).
18. Nagy, J. A. et al. Permeability properties of tumor surrogate blood vessels induced by VEGF-A. *Lab. Invest.* **86**, 767–780 (2006).
19. Feng, D. et al. Reinterpretation of endothelial cell gaps induced by vasoactive mediators in guinea-pig, mouse and rat: many are transcellular pores. *J. Physiol.* **504**, 747–761 (1997).
20. Feng, D. et al. Pathways of macromolecular extravasation across microvascular endothelium in response to VPF/VEGF and other vasoactive mediators. *Microcirculation* **6**, 23–44 (1999).
21. Dvorak, H. F., Nagy, J. A., Dvorak, J. T. & Dvorak, A. M. Identification and characterization of the blood vessels of solid tumors that are leaky to circulating macromolecules. *Am. J. Pathol.* **133**, 95–109 (1988).
22. Feng, D., Nagy, J. A., Dvorak, H. F. & Dvorak, A. M. Ultrastructural studies define soluble macromolecular, particulate, and cellular transendothelial cell pathways in venules, lymphatic vessels, and tumor-associated microvessels in man and animals. *Microsc. Res. Tech.* **57**, 289–326 (2002).
23. Neal, C. R. & Michel, C. C. Transcellular openings through frog microvascular endothelium. *Exp. Physiol.* **82**, 419–422 (1997).
24. Michel, C. C. & Neal, C. R. Openings through endothelial cells associated with increased microvascular permeability. *Microcirculation* **6**, 45–54 (1999).
25. Syed, A. M. et al. Three-dimensional imaging of transparent tissues via metal nanoparticle labeling. *J. Am. Chem. Soc.* **139**, 9961–9971 (2017).
26. Sindhwani, S., Syed, A. M., Wilhelm, S. & Chan, W. C. W. Exploring passive clearing for 3D optical imaging of nanoparticles in intact tissues. *Bioconjug. Chem.* **28**, 253–259 (2017).
27. Sindhwani, S. et al. Three-dimensional optical mapping of nanoparticle distribution in intact tissues. *ACS Nano* **10**, 5468–5478 (2016).
28. Ramanujan, S. et al. Diffusion and convection in collagen gels: implications for transport in the tumor interstitium. *Biophys. J.* **83**, 1650–1660 (2002).
29. Sykes, E. A. et al. Tailoring nanoparticle designs to target cancer based on tumor pathophysiology. *Proc. Natl Acad. Sci. USA* **113**, E1142–E1151 (2016).
30. Schnitzer, J. E. gp60 is an albumin-binding glycoprotein expressed by continuous endothelium involved in albumin transcytosis. *Am. J. Physiol. Heart Circulatory Physiol.* **262**, H246–H254 (1992).
31. Schnitzer, J. E. in *Whole Organ Approaches to Cellular Metabolism* (eds Bassingthwaighte, J., Goresky, C. A., Linehan, J. H 31–69 (Springer, 1998).
32. Oh, P. et al. In vivo proteomic imaging analysis of caveolae reveals pumping system to penetrate solid tumors. *Nat. Med.* **20**, 1062–1068 (2014).
33. Thurston, G. et al. Cationic liposomes target angiogenic endothelial cells in tumors and chronic inflammation in mice. *J. Clin. Invest.* **101**, 1401–1413 (1998).
34. McDonald, D. M. Uptake of cationic liposomes by normal and angiogenic endothelial cells in vivo. *Nat. Biotechnol.* **17**, 14–14 (1999).
35. Tkachenko, E. et al. Caveolae, fenestrae and transendothelial channels retain PV1 on the surface of endothelial cells. *PLoS ONE* **7**, e32655 (2012).
36. Stan, R. V., Tkachenko, E. & Niesman, I. R. PV1 Is a key structural component for the formation of the stomatal and fenestral diaphragms. *Mol. Biol. Cell* **15**, 3615–3630 (2004).
37. Stan, R. V. et al. The diaphragms of fenestrated endothelia: gatekeepers of vascular permeability and blood composition. *Dev. Cell* **23**, 1203–1218 (2012).
38. Dai, Q. et al. Quantifying the ligand-coated nanoparticle delivery to cancer cells in solid tumors. *ACS Nano* **12**, 8423–8435 (2018).
39. Qaddoumi, M. G. et al. Clathrin and caveolin-1 expression in primary pigmented rabbit conjunctival epithelial cells: role in PLGA nanoparticle endocytosis. *Mol. Vis.* **9**, 559–568 (2003).
40. Voigt, J., Christensen, J. & Shastri, V. P. Differential uptake of nanoparticles by endothelial cells through polyelectrolytes with affinity for caveolae. *Proc. Natl Acad. Sci. USA* **111**, 2942–2947 (2014).
41. Ho, Y. T., Kamm, R. D. & Kah, J. C. Y. Influence of protein corona and caveolae-mediated endocytosis on nanoparticle uptake and transcytosis. *Nanoscale* **10**, 12386–12397 (2018).
42. Chauhan, V. P. et al. Normalization of tumour blood vessels improves the delivery of nanomedicines in a size-dependent manner. *Nat. Nanotechnol.* **7**, 383–388 (2012).
43. Schubert, W. et al. Caveolae-deficient endothelial cells show defects in the uptake and transport of albumin in vivo. *J. Biol. Chem.* **276**, 48619–48622 (2001).
44. Matsumoto, Y. et al. Vascular bursts enhance permeability of tumour blood vessels and improve nanoparticle delivery. *Nat. Nanotechnol.* **11**, 533–538 (2016).
45. Naumenko, V. A. et al. Extravasating neutrophils open vascular barrier and improve liposomes delivery to tumors. *ACS Nano* **13**, 12599–12612 (2019).
46. Harney, A. S. et al. Real-time imaging reveals local, transient vascular permeability, and tumor cell intravasation stimulated by TIE2hi macrophage-derived VEGFA. *Cancer Discov.* **5**, 932–943 (2015).

Methods

Materials. All the materials were obtained from Sigma-Aldrich unless otherwise mentioned.

Preparation of AuNPs. AuNPs were prepared using previously established reduction methods in our lab[47,48]. We used 15 nm AuNPs as seeds to make larger AuNPs (50 and 100 nm). The 15 nm AuNPs were synthesized by first boiling and stirring 100 ml of 0.25 mM chloroauric acid (Sigma). Then 1 ml of 3.3% w/v aqueous sodium citrate dibasic trihydrate was added to this solution, which subsequently reduced chloroauric acid. The solution changed colour from dark purple colour to bright red over 10 min. This solution was cooled to room temperature. The 15 nm AuNPs were then characterized for their size and concentration using dynamic light scattering and ultraviolet–visible absorbance spectroscopy, respectively[47,48]. To prepare the 50 nm AuNPs, 967 µl of 25 mM chloroauric acid (Sigma), 93.75 ml of deionized water, 967 µl of 15 mM sodium citrate tribasic dehydrate and 3.35 ml of 2.4 nM 15 nm AuNP seeds were mixed and stirred overnight. Similarly, to prepare the 100 nm AuNPs, 997 µl of 25 mM chloroauric acid (Sigma), 96.7 ml of deionized water, 997 µl of 15 mM sodium citrate tribasic dehydrate and 0.305 ml of 2.4 nM 15 nm AuNP seeds were mixed and stirred overnight. Both of these reactions to increase size can be scaled up tenfold by increasing the concentrations of the components by tenfold without increasing the deionized water volume. The next day, Tween 20 was added to these reactions at a final concentration of 0.05% v/v. This stabilizes the AuNPs during centrifugation. The 50 nm and 100 nm AuNPs were concentrated by centrifuging for 2 h in 50 ml Falcon tubes at 2,000 and 1,000*g*, respectively. Concentrated stocks were kept at 4 °C until PEGylation.

Preparation of PEGylated AuNPs. The PEGylation of AuNPs refers to nanoparticle surface conjugation with PEG. For all three AuNP sizes (15, 50 and 100 nm), this was done using thiol chemistry, as described previously[25,26,29,38,49]. Methoxy-PEG-thiol (mPEG, 5,000 Da; Laysan Bio) was dissolved in deionized water at 10 mg ml^{-1}. This solution was added to AuNPs (dispersed in 0.05% Tween 20) such that the ratio of PEG to the AuNP surface was 5 PEG molecules nm^{-2} of the nanoparticle surface area. This reaction was done at 60 °C for 1 h. Unconjugated excess PEG was removed by centrifuging the AuNPs, at the same speed as mentioned above, three times with PBS. These PEGylated AuNPs were stable and stored at 4 °C.

Injection of PEGylated AuNPs into mice. The PEGylated AuNPs were injected intravenously, using a 29 gauge insulin syringe, into mice at doses of 2×10^{12} AuNPs (100 nm), 2×10^{13} AuNPs (50 nm), 1×10^{14} AuNPs (15 nm). All of these injections were done by dispersing the required AuNPs in 150 µl of PBS.

Mice tumour models. Four different mouse tumour models were used in this work: U87-MG, 4T1, PDX and MMTV-PyMT.

U87-MG. This xenograft tumour was developed by injecting 5–7 million cells in 200 µl of a 50:50 PBS:Matrigel solution into the subcutaneous area in the right flank of the CD1 Nude mouse (Charles River Canada). The tumour was allowed to grow to 1 cm^3 over 4–6 weeks.

4T1. This syngeneic tumour was developed by injecting two million cells in 200 µl of a 50:50 PBS:Matrigel solution into the mammary fat pad of BALB/c mouse (Charles River Canada). The tumour was allowed to grow to 400–600 mm^3 over 4–6 weeks.

PDX. The PDX Triple Negative Breast Cancer (TNBC) tumours (HCI-002) were sectioned into ~2×4 mm chunks and surgically implanted within NOD-SCID (Charles River Canada) mice within the mammary fat pad. The rationale for using the PDX model here was threefold. First, it allowed us to preserve the tumour microenvironment from the patient and include cells such as fibroblasts, macrophages and immune cells while implanting the tumour. Second, it allowed us to develop a cancer model from a cell line that has not undergone years of passage, as is the case in xenograft models. This means that the cancer cells implanted have fewer mutations and are more representative of the patient. Lastly, the PDX model of breast cancer allowed us to examine breast cancer across three different tumour implantation models—orthotopic syngeneic (4T1), PDX and MMTV-PyMT (genetically engineered mouse model).

MMTV-PyMT. This genetically engineered mouse model was graciously donated by M.E. (Cold Spring Harbor Laboratory). This has been previously used by their lab for visualizing the tumour microenvironment[50].

Purpose of 3D imaging and TEM. Images from TEM were analysed manually to count the gap frequency. This was done because gaps cannot be visualized by 3D optical microscopy due to the diffraction limit of light. 3D optical microscopy provided a qualitative evaluation of large-volume staining for markers related to the blood vessel structure.

Transcardial perfusion fixation for 3D imaging. Perfusion procedures were the same as published previously[25–27]. We also conjugated Unconjugated Griffonia Simplicifolia Lectin I (Vector Labs, Catalogue no. L-1100) to Sulfo-Cy3-NHS (Click Chemistry Tools, Catalogue no. 1075-25) using previously established methods[25–27]. GSL1-Cy3 (0.15 ml of 1 mg ml^{-1}) was injected intravenously via the tail vein to label the mouse vasculature. This was allowed to circulate for 5 min. Mice were then anaesthetized under a continuous flow of 3% isoflurane in oxygen. Surgical procedures to access heart the were performed by opening the ribs and dissecting along the sides. The needle was inserted in the left ventricle and 60 ml of PBS solution that contained 10 U ml^{-1} Heparin (Bioshop Canada Inc.) and 0.5% w/v sodium nitrite (Sigma Aldrich) in 1× PBS was injected at a constant flow rate of 5–7 ml min^{-1}. Next, 60 ml of monomer solution was infused at the same flow rate. This monomer solution was made of 4% formaldehyde (Bioshop Canada Inc.), 2% acrylamide (Bioshop Canada Inc.) and 0.25% initiator (VA-044 azoinitiator, Wako Chemicals) in 1× PBS solution. After perfusion, the desired organs were resected and incubated in the same monomer solution at 4 °C for another 7 days.

Tissue cross-linking for 3D imaging. After 1 week of incubation with the monomer solution, the tissues were cross-linked by following procedures as per previously published work[25–27]. The monomer solution was replaced with fresh 20 ml of the same solution. Fresh frozen human samples were also processed in a similar way and transferred to 20 ml of monomer solution. The samples were degassed and purged with argon three times. During these cycles, the caps on the falcon tubes were perforated. This removed most of the oxygen and the tubes were sealed by tightening the caps and wrapping with parafilm over the top. The samples were polymerized at 37 °C with shaking for 3 h. The solution was viscous due to cross-linking at the end of this cycle. Excess solution was removed and gelled tissues were rinse with deionized water and then stored in 10 ml of borate buffer (200 mM sodium borate, pH 8.5, 0.1% Triton-X100 and 0.01% sodium azide) at 4 °C.

Tissue clearing. Tissues were cleared passively as established previously[25–27]. After the gelling in the previous step, tissues were placed in the clearing solution (4% w/v sodium dodecyl sulfate and 200 mM sodium borate at pH 8.5) for 2 weeks at 50 °C using 15 ml of clearing solution for 1–2 mm slices. Once cleared, these were stored at 4 °C in borate buffer.

3D tissue immunostaining. Staining involved blocking and the use of primary and secondary antibodies. Details regarding these antibodies are listed in Supplementary Table 9. Non-specific staining was reduced by first blocking the cleared tissues with 5% w/v bovine serum albumin in 1× PBS, 0.1% Triton-X 100 and 0.01% sodium azide solution overnight at room temperature with gentle agitation. The tissues were then incubated with primary antibody at room temperature for 3 days in a solution that contained 1 ml of 2% v/v goat serum, PBS, 0.1% Triton-X 100 and 0.01% sodium azide at a specific dilution (Supplementary Table 9 gives the dilutions). The tissue was then washed three times with 10 ml of PBS, 0.1% Triton-X 100 and 0.01% sodium azide solution over a period of 24 h at room temperature. The tissue was then stained with secondary antibody at room temperature for 3 days in a solution that contained 1 ml of 2% v/v goat serum, PBS, 0.1% Triton-X 100 and 0.01% sodium azide at a specific dilution (Supplementary Table 9 gives the dilutions).The tissue was then washed three times with 10 ml of PBS, 0.1% Triton-X 100 and 0.01% sodium azide solution over a period of 24 h at room temperature. The tissue was transferred into 67% 2,2′-thiodiethanol solution in 200 mM borate, 0.1% Triton-X and 0.01% sodium azide solution for refractive index matching. This was done a day before imaging to make a homogeneous refractive index inside the tissues.

Transcardial perfusion fixation for TEM. This procedure is same as that described above in the Transcardial perfusion fixation for 3D imaging except that only one solution, the TEM solution (4% formaldehyde and 0.5% glutaraldehyde in 1× PBS), was infused instead of PBS or monomer solution. This was followed by storing the sample in the TEM solution at 4 °C until sample preparation for TEM.

Zombie fixation and nanoparticle circulation. Zombie was developed by first fixing the whole mouse using transcardiac perfusion with the TEM solution (4% formaldehyde and 0.5% glutaraldehyde in 1× PBS) for 20 min. Supplementary Video 1 shows our set-up with a box, pump and circulation. The fixed animal was then placed inside the box for 1 h of further fixation at 37 °C. The box was closed and sealed to avoid any evaporation. After 1 h, the fixative was removed, the box was washed and nanoparticle solution was added for circulation. The concentration of this nanoparticle solution was same as that in the control animal assuming 1.8 ml of blood. To do this, we added a fivefold amount of nanoparticles in 9 ml of either PBS or 100% serum solution (CD1 nude mouse serum, Innovative Research). An additional condition was also tested in which nanoparticles were fivefold the amount of nanoparticles in 9 ml, a solution that contained 55% serum (CD1 nude mouse serum, Innovative Research) and 45% red blood cells (CD1 nude mouse red blood cells, Innovative Research by volume. This was done to mimic blood. Each of these nanoparticle solutions was then circulated in the fixed mouse at a physiologically relevant flow (5–7 ml min^{-1}) rate using a peristaltic pump that alters the pressure during circulation. The circulation lasted for 4 h for

PEGylated 15 s, and 50 s and 1 h for PEGylated 100 nm AuNPs. The tumours were then resected from these mice and processed for TEM and ICP-MS.

Zombie fixation for 3D imaging. We modified the procedure for 3D imaging of Zombie mice because the initiator that cross-links the tissue to form the hydrogel before clearing is activated by temperature. The goal of doing 3D imaging with the Zombie mice was to visualize the distribution of nanoparticles when the active pathways were not present. We started the procedure by injecting the animal with Cy3-labelled GSL-1 intravenously. After 5–10 min, we proceeded with the transcardiac perfusion procedure for 3D imaging. We perfused the animal with 60 ml of a PBS solution that contained heparin and sodium nitrite (see above). Then, we perfused it with 60 ml of the hydrogel monomer solution without the VA-044 initiator (4% formaldehyde and 2% acrylamide in 1× PBS). This was done to fix the proteins in place without polymerizing the acrylamide hydrogel. We then circulated AuNPs (incubated in serum to mimic physiological conditions) through the fixed mice. After this round, we then circulated the monomer solution with the initiator similarly to that for the 3D imaging processing and kept the tissues for a week incubating with the same solution. The rest of the procedure for the 3D imaging of Zombie mouse was same as described in the section above.

Quantification of nanoparticle accumulation and pharmacokinetics using ICP-MS. The gold content inside any organ can be measured using ICP-MS. This was carried out using established procedures published previously[25,26,38]. Tumours were resected, weighed and placed in 50 ml Falcon tubes. They were then digested with 2 ml of nitric acid (ACS grade, Caledon) and 0.5 ml of hydrochloric acid (ACS grade, Caledon) at 70–80 °C overnight. The tissues appeared digested and dissolved. The samples were diluted to 50 ml with deionized water and then filtered with 0.22 µm PES filters (Millipore) using a 10 ml syringe. The filtered digest was then processed using ICP-MS and analysed using a standard curve derived from stock with a known quantity of gold.

The concentration inside the Zombie model remained the same because the circulation maintains a fixed amount in a given volume circulating through the animal with no active ongoing processes. This does not capture the exponential decay in concentration of nanoparticles that occurred in the control tumour-bearing mice. Thus, the nanoparticle accumulation measured in the tumours of Zombie mice using ICP-MS requires a correction factor that accounts for the decreasing blood correction of a control animal. To do this, we performed pharmacokinetics of AuNPs by collecting and digesting blood samples from mice at eight time points within the first 24 h. Blood (0.01–0.05 m) was collected from the tail of mice and stored in Eppendorf tubes. The blood was digested with 0.5 ml of nitric acid (ACS grade, Caledon) and 0.1 of hydrochloric acid (ACS grade, Caledon) at 70–80 °C for 1 h. This was transferred to a 15 ml tube and diluted to 10 ml. Filtration and gold measurement was done as described in the paragraph above. After obtaining the blood concentrations of nanoparticles, we found how many AuNPs remained in the blood of a control mouse at a particular time t and then divided it by the amount that was in the Zombie mice (constant concentration). This gave us the correction factor. Thus, the formula for the corrected nanoparticle accumulation due to passive pathways (passive NP) that account for the decaying nanoparticle concentration in the blood model is:

$$\text{Passive NP}^{\text{Zombie}}_{\text{tumour at } t} = \text{Measured NP}^{\text{Zombie}}_{\text{tumour at } t} X \frac{\text{AUC}_{\text{Control blood at } t}}{\text{AUC}_{\text{Zombie blood at } t}} \quad (1)$$

where $X^{Y}_{Z \text{ at } t}$ = amount of X in Z organ of Y mice at time t

Supplementary Table 6 gives the analysed results.

Patient tumour sample acquisition. Sections (1–2 mm) of human patient biopsies were obtained from the Ontario Tumour Bank. The protocol was approved by the Research Ethics Board at the University of Toronto. The protocol ID is 34558. All the required guidelines with respect to sample handling and confidentiality were followed. After receiving the samples, they were fixed in the TEM solution (4% formaldehyde and 0.5% glutaraldehyde) for 1–2 days before being sent to the Electron Microscopy Facility at the Peter Gilgan Centre for Research and Learning for further sample preparation.

Sample preparation for TEM. Samples for TEM were prepared by D. Holmyard at SickKids Hospital, who had no knowledge of the sample parameters and sectioned randomly. This ensured the removal of any bias in the sample processing. Samples handed to the facility were in a solution of 4% formaldehyde and 0.5% glutaraldehyde in 1× PBS (TEM solution). The facility then fixed the tumour in 2% glutaraldehyde in a 0.1 M sodium cacodylate buffer, rinsed with buffer, postfixed in 1% osmium tetroxide in buffer, dehydrated in a graded ethanol series followed by propylene oxide, and embedded in Quetoi-Spurr resin. Next, sections of thickness 90 nm were cut on a Leica Ultracut ultramicrotome, stained with uranyl acetate and lead citrate, and digitally imaged using a FEI Tecnai 20 TEM.

Analysis of TEM images. The variables of interest were tumour type (4T1, MMTV, U87, PDX and human), time point (15 min, 1 h), particle size (15, 50 and 100 nm). the categories measured were blood vessel features (tight junction, fenestrae and intercellular gap or intracellular gap).

Manual annotation of TEM images. Images acquired from TEM were stored on a central server. For each organ analysed, we selected at least seven tiled images for annotation. These tiled images contained between 1 and 120 fields of view depending on the size of the blood vessel. Each image contained one vessel to be analysed for its features related to the endothelium (such as tight junctions, fenestrae, intercellular gaps and intracellular gaps) and the number of nanoparticles relative to the location within the vessel.

We undertook several measures to remove sources of bias. First, each researcher was trained through seminars to recognize the nine features we wanted to annotate: nanoparticles in the blood vessel lumen, on the sidewall, in the endothelial cell vesicle, in the endothelial cell cytoplasm and in extravascular space, and tight junctions, fenestrae, inter-endothelial cell gaps and transcellular channels. Second, we tested the researchers who performed the annotations on two test datasets and provided them feedback on their accuracy before they began labelling the final data. Third, we assigned each vessel image randomly to three independent researchers who did not interact with each other while annotating the images. This ensured the removal of any bias and increased the accuracy due to triplicate measurements. Previous studies did not analyse the data in this manner. Fourth, we provided each researcher with a custom set of FIJI macros and scripts that created an interactive annotation process. The researcher would identify a feature, click on it and press a shortcut key to create a circular annotation that identified the feature (and modified the image at that circle with a numerical value that corresponded to the feature). The annotations were then immediately visible to the user as a colour-coded circle (colours were assigned using a custom lookup table) to indicate the what kind of feature it was, such as a tight junction on an endothelial cell or a nanoparticle within the lumen. Fifth, we analysed these annotated images through an automated image analysis pipeline to reduce bias and error when counting thousands of particles. These measures ensured the robustness of quantification. Supplementary Fig. 5 gives the flowchart of analysis.

Image analysis of manually annotated TEM images. After annotation by three independent researchers we analysed these images in MATLAB. We obtained a count of each feature by analysing these features from the annotated images. The images to be annotated were rescaled to have intensities between 0 and 235 with all the values greater than 235 corresponding to manual annotations. Each annotated feature had a unique intensity value; for example, nanoparticles in the lumen were labelled with circles with an intensity of 246. For each feature, we extracted only pixels that contained the corresponding intensity value. We then separated overlapping annotations using a watershed segmentation and counted the number of regions to quantify the number of instances of each feature in the image for each of the triplicate annotated images.

Consensus gaps and quantification of other features. Most of these features are unambiguous in the TEM images with the exception of endothelial cell gaps. To improve the accuracy of this count for the measurement of gaps we collected all the images that had been labelled by at least one researcher as having any type of gap. We reviewed these images one by one and held a vote to determine whether each gap was a transcellular channel, an inter-endothelial gap, a misannotation, an imaging artefact or one of the other features. The revised consensus gaps were re-annotated on the images as new features. For all the other features, we chose the median count from each category counted between the three independent researchers of the same blood vessel. The median was calculated within each image in bins going around the blood vessel (Spatial correlation analysis section). These features were tabulated based on the counts measured for the categories (blood vessel features and nanoparticle location) and organized based on the variables tested (tumour type, particle size and time point). Median numbers for each feature were analysed either based on the vessel feature or nanoparticle location.

For instance, to calculate the frequency of tight junctions per millimetre of blood vessel perimeter measured within U87 tumours, the number of tight junctions measured per vessel was divided by the perimeter of a vessel. The mean was calculated across all the vessels imaged from U87 tumours. This is the mean reported in Supplementary Tables 1 and 8. The associated s.d. for each feature for a particular tumour type was calculated assuming a Poisson distribution, $\sqrt{\text{mean} \times \text{vessel perimeter}}/\text{vessel perimeter}$.

For instance, to calculate the percentages for 50 nm, 30 min, 4T1 we would first take all six images from the first replicate mouse of that condition. We would sum all the nanoparticles within these six images and calculate the percentage in the lumen, or frequency of nanoparticle per cross-sectional area and so on. Then, these calculations would be repeated for each of the replicate animals and values from each replicate would be used to derive the mean and s.d. These results are reported in Supplementary Table 2.

Spatial correlation analysis. To quantify whether the presence of any type of feature was correlated with extravascular nanoparticles, we analysed the correlation with respect to the blood vessel. We traced the outline of each blood vessel and marked it as a new annotation. We loaded this vessel annotation in MATLAB and identified the perimeter of the blood vessel. We divided this perimeter into ten equal segments and all the extravascular nanoparticles and endothelial cell features were then assigned the nearest perimeter segment. Collected over all images, we

then evaluated the Spearman correlation coefficient, ρ, of each type of blood vessel feature against the number of extravascular nanoparticles present in its proximity.

Measurement of length and surface area for blood vessel and gaps. To determine the total length of the blood vessels examined, we measured the major axis Feret diameter of each traced blood vessel. To measure the surface area of the blood vessels, we calculated the perimeter of the traced vessel and multiplied it by the thickness of the slice (90 nm). To determine the surface area of the gaps, we measured the length of each annotated gap and multiplied it by the thickness of the slice.

Mathematical modelling of extravasation and comparison with intratumoural accumulation of nanoparticles. To determine if the observed number of holes was sufficient to explain the observed accumulation, we simulated the distribution of nanoparticles in the tumour. Previous models of nanoparticle transport were limited because they could not account for the organization of the blood vessel architecture and density in the tumour. We performed 3D microscopy of U87-MG tumours and visualized the blood vessel architecture using GSL1-Cy3. The tissue processing and staining methods are explained in detail in previous sections. Tissue slices were imaged using a Zeiss Lightsheet Z.1 microscope at an isotropic resolution of 2 µm and a field of view of 1.2 mm in all dimensions. The blood vessel images were segmented using a manually trained random forest algorithm implemented in Ilastik. Binary segmented blood vessel images were used for diffusion simulations.

Mathematical formulation of diffusion simulation. The dynamics of nanoparticles in the tumour can be described using the diffusion equation:

$$\frac{\partial n}{\partial t} + \nabla(\mathbf{v}n(\mathbf{x},t)) = D\nabla^2 n(\mathbf{x},t) + R(n(\mathbf{x},t),\mathbf{x},t) \quad (2)$$

where $\mathbf{v}$ is a velocity field. Short of being able to solve this analytically, we numerically simulated this partial differential equation using a Euler method on a cubic lattice.

The upper limit of D was calculated using the Stokes–Einstein equation:

$$D = \frac{k_B T}{6\pi\eta r} \quad (3)$$

where k_B is the Boltzmann constant, T the absolute temperature, η the dynamic viscosity and r the radius of the spherical particle. Using the dynamic viscosity of blood $\eta = 2.87\,\mathrm{mPa\,s^{-1}}$ and room temperature, we estimated the diffusion coefficient in blood to be $D \leq 1.5\,\mu\mathrm{m^2\,s^{-1}}$. In the tumour microenvironment, D is further limited by the collagen concentration. Previous experimental measurements of D estimated it to be around $0.05\,\mu\mathrm{m^2\,s^{-1}}$, which is what we used[28].

We assumed that the contribution of a velocity field to the dynamics of the nanoparticles was negligible. Effectively, we set $\mathbf{v} = 0$. Vasculature images obtained through the CLARITY technique were segmented to obtain vasculature data that we could use in our simulations (images available at https://doi.org/10.6084/m9.figshare.7485770). Neumann boundary conditions were set along the vasculature so that particles did not enter or exit through the endothelial cells, $\nabla n(\mathbf{x},t) = 0$.

Locations along the vasculature were randomly selected for the fenestrae. The source terms in our equation are those holes that provide the diffusive flow of particles from inside the vessels to the tumour microenvironment. The concentrations at these hole locations were set to be equal to the observed concentrations inside the vessels as a function of time, that is:

$$n_0(t) = 0.5407\mathrm{e}^{-0.3465t} + 0.4593\mathrm{e}^{-5.122t} \quad (4)$$

This equation was fitted from the normalized observed pharmacokinetics of nanoparticles in CD1 nude mice that bore U87-MG tumours. Simulations were run to obtain the concentration profiles at 30 min postinjection, with time steps of 0.25 s.

All the code for these simulations can be found at https://github.com/jbRothschild/nano-extravasation.

Comparison of accumulation in observed versus simulated distributions. Accumulation in the simulated tumour images was determined by taking the mean numerical value of the voxels in the simulated image and multiplying it by the normalization factor of the pharmacokinetic curve, 55% ID g^{-1}, which gives the concentration of particles in the tumour microenvironment. The total accumulation in the tumour was determined by multiplying this value by 1 g because this was the standard tumour size used in this study.

Effect of caveolin-1 knockout on nanoparticle tumour accumulation. Age-matched Cav-1 knockout (stock no. 007083, strain B6.Cg-Cav1/J) and control C57Bl/6J (stock no. 000664, strain C57BL/6J) mice were ordered from Charles River. B16.F10 melanoma tumours were induced by injecting 200,000 cells suspended in 0.2 ml of PBS into the right flank of the mice. At 2 weeks post-tumour induction, 2×10^{13} 50 nm PEGylated AuNPs were injected intravenously into these tumour-bearing mice via the tail vein. The nanoparticles were circulated for 4 h and the organs were dissected from mice for acid digestion and processing. The nanoparticle accumulation in organs was measured using ICP-MS using the same procedure as described above.

Effect of tumour vessel normalization. Age-matched CD-1 nude mice were ordered from Charles River and U87-MG glioblastoma tumours were induced as described above. At 3 weeks post-tumour induction, the tumour vessel normalization protocol was induced by intravenous injection of 5 mg kg^{-1} DC101 via the tail vein and left for 2 days. This is in accordance with work from the Jain lab. Next, 2×10^{12} 50 nm PEGylated AuNPs were injected intravenously into these tumour-bearing mice via the tail vein. the nanoparticles were circulated for 4 h and organs were dissected from mice for acid digestion and processing. The nanoparticle accumulation in organs was measured using ICP-MS using the same procedure as described above.

Intravital imaging. *Mammary tumour MMTV-PyMT Mice.* Intravital microscopy for MMTV-PyMT mice was performed as described previously[51]. Briefly, 150 µl of a 1 mg ml^{-1} GSL1-Cy3 solution was injected into the mice via the tail vein to label blood vessels. Then, the mice were anaesthetized with 4% isoflurane (at 21% oxygen, balance nitrogen) and surgery was performed with 2.5% isoflurane. The ventral surface of the mouse was prepared for surgery with isopropyl alcohol and a ventral midline incision was then made with sterilized scissors. The inguinal mammary fat pad was surgically exposed and a glass microscope slide was glued to the skin behind the mammary gland. The glass slide was rotated to expose the inner surface of the mammary gland, and the mouse was transferred to the microscopic stage. During imaging, isoflurane was reduced to the lowest concentration at which the mouse did not react to pain. We used an oximeter probe (MouseOx, Starr Life Sciences,) to monitor and display the heart rate (beats per minute), the arterial oxygen saturation of the blood (%) and the distension of blood vessels (µm) caused by the pulse and breathing. This real-time feedback allowed us to adjust the anaesthesia levels to the individual mouse. During the imaging procedure, isoflurane was delivered in a humidified mix of nitrogen and oxygen (at least 21%), with oxygen adjusted to achieve a >95% oxygen saturation of the arterial blood as measured with an oximeter probe. Mice received 50–100 µl h^{-1} of saline intraperitoneally and were covered with a recirculating heated water blanket during imaging. The 50 nm AuNPs were synthesized as above. These nanoparticles were labelled with Alexa Fluor 647 using protocols published before[52,53]. Of these Alexa Fluor 647-labelled AuNPs, 1×10^{12} were injected intravenously into the mice via the tail vein. Imaging was performed using a custom microlensed spinning disk confocal microscope (Solamere Technologies) equipped with an ICCD camera (XR-Mega-10EX S-30, Stanford Photonics), 405, 488, 561 and 647 nm solid-state laser lines and selective emission filters. Images were collected at 60 s intervals with exposure times of ~330 ms.

4T1 Mammary tumours. This syngeneic tumour model was generated by injecting 1 million 4T1 cells in BALB/c mice (6 weeks old). The injection site was the fifth inguinal mammary fat pad. The tumour was allowed to grow for 14 days. On the day of imaging, the hair was removed using a shaver. Before putting the mice on the microscope stage for imaging, 150 µl of a 1 mg ml^{-1} GSL1-Cy3 solution was injected via the tail vein to label blood vessels. Immediately thereafter, the mouse was anaesthetized with isoflurane at 5% isoflurane in oxygen, initially in a chamber and then transferred to a supine position with a nose cone at 2.5% isoflurane in 0.5 l min^{-1} oxygen for anaesthesia maintenance. In the supine position, the legs and arms were immobilized to the stage by using tape. A heat lamp was used to maintain the body temperature, which was monitored using a rectal probe. The tumour was exposed by making incisions around it and peeling it off away from the peritoneum. Care was taken to not cause any vasculature injury. The skin that surrounded the tumour was used to pin down the tumour using needles. The tumour was wetted with a few drops of PBS and then a coverslip was placed on top and taped. This liquid layer avoided vessel collapse and maintained the refractive index. The stage could be moved in *XY*. The microscope used for this imaging was an upright Zeiss LSM 710 confocal microscope with a ×20 water-immersion Plan Apochromat objective lens with a 1.0 numerical aperture. It could be moved in the Z axis. A drop of water was put on the glass slide. Then, the objective was brought to the glass slide to be immersed. The laser power was set to 5–10% and the signal-to-noise ratio was maximized by adjusting the gain. Other parameters were pinhole size of 1 Airy unit, acquisition rate of 1 image per second with a resolution of 512×512 pixels (without averaging). The scanning was one-directional scanning and laser speed was the maximum. The 50 nm AuNPs were synthesized as above. These nanoparticles were labelled with Alexa Fluor 647 using protocols published before[52,53]. Of these Alexa Fluor 647 labelled AuNPs, 1×10^{12} were injected intravenously into the mice via the tail vein.

Measurement of *D* in collagen before and after fixation. Collagen solutions (5 mg ml^{-1}) that contained 1.25×10^{11} AuNPs and 50% DMEM complete were prepared in a 1.6 ml semi-micro cuvette (Biomart). Gels were formed at 37 °C for 1 h. The fixation sample was then incubated with an additional 2 ml of TEM

fixative (4% formaldehyde, 0.5% glutaraldehyde, 1× PBS and 1 μg ml^{-1} of Cy3) overnight to fix the collagen. Samples without fixation were incubated with PBS. Collagen was assumed to be fixed when the Cy3 front reached the bottom of the gel. *D* was then measured using a Malvern Zetasizer instrument with 30 s acquisition time.

Sample-size simulations. A 3D microscopy image of a U87-MG xenograft tumour was thresholded for GSL1 positive blood vessels using Ilastik. The resulting image was cropped to 300×300×300 voxels and then supersampled to 600×600×600 voxels to provide a resolution of 1 μm in all dimensions. Gaps were simulated in MATLAB using three distribution scenarios: first, an even distribution in which gaps were randomly chosen from all the surface voxels in the blood vessel network; second, a localized distribution in which two points were randomly chosen on the blood vessel surface and all the gaps were randomly assigned to surface voxels within 50 μm of the original two points; third, clusters of 50 points were randomly chosen on the blood vessel surface and all the gaps were randomly assigned to surface voxels within 10 μm of any clustering point. Distributions are shown in the section Statement on sampling in Supplementary Discussion. the vessel network was skeletonized using the Skeleton3D plugin for MATLAB (www.mathworks.com/matlabcentral/fileexchange/43400-skeleton3d). Points on the skeleton were randomly chosen as locations of a TEM slice and 20 μm x 20 μm sections were analysed for the presence of a gap. To estimate the coefficient of variance of 10 vessels, 10 vessels were tested to derive an estimate of the gap density and then this process was repeated 300 times to measure the coefficient of variance of that estimate. The entire procedure was then repeated for 20 vessels, 30 vessels, … to 1,000 vessels. As we actually examined 380 vessels, the coefficient of variance we should expect is about 0.25, which means that we observed 27 gaps with a s.d. of ~5 gaps.

Statistical analysis. Prism (GraphPad Software) and MATLAB were used for the data analysis and graph plotting. All the scatter plot data are expressed as mean ± s.d. A two-way analysis of variance with a Sidak's multiple comparisons test was used to determine the statistical significance of the gold and platinum content in the Zombie and control animals (Fig. 4a). The degree of freedom was 3 and the *F* value was 1.772. The exact sample sizes for each figure that required statistical analysis are summarized in Supplementary Tables 10 and 11.

The spatial correlation coefficient was determined using the Spearman correlation analysis in MATLAB. In total, 126 vessels were analysed. The rest were excluded due to (1) no extravascular nanoparticles, (2) no Zombie experiment images and/or (3) TEM images at 1 h instead of 0.25 h (the correlation is weaker at longer time points). Spearman ρ and *P* values are given in Supplementary Table 12.

Ethics statement. All the experiments that involved animal procedures and human sample acquisition were conducted in accordance with the animal use protocols approved by the University of Toronto.

Reporting summary. Further information on research design is available in the Nature Research Reporting Summary linked to this article.

Data availability

All the annotated and analysed TEM images are uploaded on the Figshare server. This includes an Excel sheet that summarizes the results and overall analysis of the TEM images. This is available at https://doi.org/10.6084/m9.figshare.7485770. 3D images used in the simulations are also stored on Figshare and will be automatically downloaded by the code used for simulations. All other datasets generated and analysed during this study are available from the corresponding author upon reasonable request.

Code availability

All code for simulations of nanoparticles in tumours can be found at https://github.com/jbRothschild/nano-extravasation.
The code for spatial analysis of nanoparticles is uploaded to Figshare at https://doi.org/10.6084/m9.figshare.7485770.

References

47. Perrault, S. D. & Chan, W. C. W. Synthesis and surface modification of highly monodispersed, spherical gold nanoparticles of 50-200 nm. *J. Am. Chem. Soc.* **131**, 17042–17043 (2009).
48. Frens, G. Controlled nucleation for the regulation of the particle size in monodisperse gold suspensions. *Nat. Phys. Sci.* **241**, 20–22 (1973).
49. Sykes, E. A., Chen, J., Zheng, G. & Chan, W. C. W. Investigating the impact of nanoparticle size on active and passive tumor targeting efficiency. *ACS Nano* **8**, 5696–5706 (2014).
50. Nakasone, E. S. et al. Imaging tumor-stroma interactions during chemotherapy reveals contributions of the microenvironment to resistance. *Cancer Cell* **21**, 488–503 (2012).
51. Egeblad, M. et al. Visualizing stromal cell dynamics in different tumor microenvironments by spinning disk confocal microscopy. *Dis. Model. Mech.* **1**, 155–167 (2008). discussion 165.
52. Chou, L. Y. T. & Chan, W. C. W. Fluorescence-tagged gold nanoparticles for rapidly characterizing the size-dependent biodistribution in tumor models. *Adv. Healthc. Mater.* **1**, 714–721 (2012).
53. Tavares, A. J. et al. Effect of removing Kupffer cells on nanoparticle tumor delivery. *Proc. Natl Acad. Sci. U. S. A.* **114**, E10871–E10880 (2017).

Acknowledgements

The authors thank D. Holmyard and A. Darbandi at SickKids Hospital (Toronto) for their help in preparing tissue grids for TEM. The authors also thank the Ontario Tumour Bank (Canada) for cooperation with the sample collection from human biopsy samples. The Canadian authors also thank the Canadian Research Chairs Program (950-223924), Canadian Cancer Society (502200 and 706286), Natural Sciences and Engineering Research Council (2015-06397 and graduate fellowships), Walter C. Sumner Memorial Fellowship (graduate fellowships), and Canadian Institute of Health Research (PJT-148848 and FDN-159932, and graduate fellowships) for funding support. M.E. thanks the Department of Defence (DoD) for grant W81XWH-14-1-0078 and is a BCRP-Era of Hope Scholar. L.M. thanks Northwell Health for funding.

Author Contributions

S.S., A.M.S. and W.C.W.C. conceived the idea, S.S., A.M.S., J.N., B.R.K., L.M., J.L.Y.W., S.W., B.O. and Z.L. performed the experiments. S.S., A.M.S., J.N., B.R.K., P.M., Y.Z., N.U.R. and T.H. annotated the TEM images. A.M.S., J.R. and A.Z. performed the computational simulations and analysis. S.G., A.S. and L.W. provided the PDX model. L.M. and M.E. provided the GEMM model. S.S., A.M.S., J.N., B.R.K., M.E. and W.C.W.C. prepared and revised the manuscript.

Competing interests

The authors declare no competing interests.

Additional information

Supplementary information is available for this paper at https://doi.org/10.1038/s41563-019-0566-2.

Correspondence and requests for materials should be addressed to W.C.W.C.

Reprints and permissions information is available at www.nature.com/reprints.

nature research

Corresponding author(s): Warren Chan

Last updated by author(s): Nov 13, 2019

Reporting Summary

Nature Research wishes to improve the reproducibility of the work that we publish. This form provides structure for consistency and transparency in reporting. For further information on Nature Research policies, see Authors & Referees and the Editorial Policy Checklist.

Statistics

For all statistical analyses, confirm that the following items are present in the figure legend, table legend, main text, or Methods section.

n/a	Confirmed	
☐	☒	The exact sample size (*n*) for each experimental group/condition, given as a discrete number and unit of measurement
☐	☒	A statement on whether measurements were taken from distinct samples or whether the same sample was measured repeatedly
☐	☒	The statistical test(s) used AND whether they are one- or two-sided *Only common tests should be described solely by name; describe more complex techniques in the Methods section.*
☐	☒	A description of all covariates tested
☐	☒	A description of any assumptions or corrections, such as tests of normality and adjustment for multiple comparisons
☐	☒	A full description of the statistical parameters including central tendency (e.g. means) or other basic estimates (e.g. regression coefficient) AND variation (e.g. standard deviation) or associated estimates of uncertainty (e.g. confidence intervals)
☐	☒	For null hypothesis testing, the test statistic (e.g. *F*, *t*, *r*) with confidence intervals, effect sizes, degrees of freedom and *P* value noted *Give P values as exact values whenever suitable.*
☒	☐	For Bayesian analysis, information on the choice of priors and Markov chain Monte Carlo settings
☒	☐	For hierarchical and complex designs, identification of the appropriate level for tests and full reporting of outcomes
☒	☐	Estimates of effect sizes (e.g. Cohen's *d*, Pearson's *r*), indicating how they were calculated

Our web collection on statistics for biologists contains articles on many of the points above.

Software and code

Policy information about availability of computer code

Data collection	No software was used for data collection.
Data analysis	MATLAB 2017b, FIJI 1.52n, Python 2.7, Graphpad Prism 7 and Bitplane Imaris 8 were used for data analysis and visualization. MATLAB scripts used for analysis and all Python scripts are provided in repositories.

For manuscripts utilizing custom algorithms or software that are central to the research but not yet described in published literature, software must be made available to editors/reviewers. We strongly encourage code deposition in a community repository (e.g. GitHub). See the Nature Research guidelines for submitting code & software for further information.

Data

Policy information about availability of data

All manuscripts must include a data availability statement. This statement should provide the following information, where applicable:

- Accession codes, unique identifiers, or web links for publicly available datasets
- A list of figures that have associated raw data
- A description of any restrictions on data availability

All the annotated and analyzed TEM images have been uploaded on the Figshare server. This includes an excel sheet summarizing the results and overall analysis of TEM images. This is available at: https://figshare.com/s/b5723a503d39e0651c14 3D images used in the simulations are also stored on Figshare and will be automatically downloaded by the code used for simulations. All other datasets generated and analyzed during this study are available from the corresponding author on reasonable request.

Field-specific reporting

Please select the one below that is the best fit for your research. If you are not sure, read the appropriate sections before making your selection.

☒ Life sciences ☐ Behavioural & social sciences ☐ Ecological, evolutionary & environmental sciences

For a reference copy of the document with all sections, see nature.com/documents/nr-reporting-summary-flat.pdf

Life sciences study design

All studies must disclose on these points even when the disclosure is negative.

Sample size	Vessel annotation: We investigated the sample size we would need to get a reasonable estimate of the gap density based on how many vessel images we analyzed. We computationally simulated the process of counting gaps from TEM images of vessels using 3D images from cleared tissues (see Supplementary Figure 10). Gaps might be distributed in one of three possible scenarios: even, clustered or localized. By simulating the observed gap density 100 times for each number of images, we derived the coefficient of variation of our gap density estimate for each number of images analyzed. For example, if we look at 400 random blood vessels and we observed 25 gaps (similar to our actual numbers), then the coefficient of variation would be ~0.2 suggesting that the standard deviation is ~5 gaps. The results of the simulations show no difference between the different gap distributions and suggest that we should examine greater than 200 images to derive a rough estimate (Coefficient of Variation <0.5) of gap density. These simulations also suggest that the type of distribution of gaps should not significantly affect the estimates of gap density (see Supplementary Figure 10). Other experiments: No statistical methods were used to predetermine sample size for other experiments.
Data exclusions	TEM images were excluded from analysis if they contained artifacts that would interfere with analysis. Specifically, we used the following pre-determined criteria for excluding images: 1) Cell membranes could not be identified due to poor staining. This is an imaging artifact. 2) Candidate vessels did not have an identifiable lumen. This is a biological artifact indicating a non-perfused blood vessel. 3) Images containing severe tiling artifacts resulting in missing information between tiles. This is an imaging artifact. All analyzed images available on Figshare repository. Full imaging dataset available upon request.
Replication	All annotated images were annotated in triplicate by three separate researchers for each image. The full record of each annotation is indicated in the raw images. Differences between researchers were minor.
Randomization	We randomly selected vessels using MATLABs "datasample" function. Specifically, we tracked
Blinding	Researchers were partially blind to the dataset. Researchers were given information about which type of nanoparticles would be present in the image to facilitate counting but were not informed about the details of the experiment.

Reporting for specific materials, systems and methods

We require information from authors about some types of materials, experimental systems and methods used in many studies. Here, indicate whether each material, system or method listed is relevant to your study. If you are not sure if a list item applies to your research, read the appropriate section before selecting a response.

Materials & experimental systems

n/a	Involved in the study
☐	☒ Antibodies
☐	☒ Eukaryotic cell lines
☒	☐ Palaeontology
☐	☒ Animals and other organisms
☐	☒ Human research participants
☒	☐ Clinical data

Methods

n/a	Involved in the study
☒	☐ ChIP-seq
☒	☐ Flow cytometry
☒	☐ MRI-based neuroimaging

Antibodies

Antibodies used	Antibody Species Tested Supplier Clone Primary dilution Secondary used Supplier Secondary dilution PV-1 Mouse Biolegend (120502) MECA-32 1:400 Goat anti-rat IgG - Alexa 647 BioLegend (405416) 1:400 PLVAP Human Abcam (ab81719) 174/2 1:100 Goat anti-mouse IgG - Alexa 647 BioLegend (405322) 1:200 VE-Cadherin Mouse/human Abcam (ab33168) Polyclonal 1:500 Donkey anti-rabbit IgG - Cy3 BioLegend (406402) 1:200
Validation	Antibody: PV-1 (Pan-endothelial cell antigen), Clone: MECA-32, Reactivity Tested: Mouse, Supplier Info: Biolegend (Product #:

120502). Validation: Antibody was tested in cleared mouse tumour tissues (U87, 4T1, MMTV-PyMT) and staining was compared to IHC staining referenced by the supplier (https://www.biolegend.com/de-at/products/purified-anti-mouse-panendothelial-cell-antigen-antibody-2967; Kopp HG, et al. 2005. Blood 106:505).

Antibody: PLVAP/PV-1, Clone: 174/2, Reactivity Tested: Human, Supplier Info: Abcam (Product #: ab81719). Validation: Antibody was tested in cleared human tumour tissues (breast, ovarian and central nervous system tumours) and staining was compared to IF staining available on the supplier website (https://www.abcam.com/plvappv-1-antibody-1742-ab81719.html). Staining was also compared to labelled vasculature in cleared human embryo samples (Belle M, et al. 2017, Cell. 169).

Antibody: VE-Cadherin, Clone: Polyclonal, Reactivity Tested: Mouse, Human Supplier Info: Abcam (Product #: ab33168): Validation: Antibody was tested in cleared human tumour tissues (breast, ovarian and central nervous system tumours) and in cleared mouse tumour tissues (U87, 4T1, MMTV-PyMT) and staining was compared to IF and IHC staining available on the supplier website (https://www.abcam.com/ve-cadherin-antibody-intercellular-junction-marker-ab33168).

Eukaryotic cell lines

Policy information about cell lines

Cell line source(s)	U87MG cells were donated by Prof. Gang Zheng at the University ofToronto. 4Tl cells were donated by Dr. Reginald Gorczynski at the University of Toronto.
Authentication	Cell lines were not authenticated.
Mycoplasma contamination	All cell lines tested negative for Mycoplasma contamination.
Commonly misidentified lines (See ICLAC register)	We did not use any commonly misidentified cell lines.

Animals and other organisms

Policy information about studies involving animals; ARRIVE guidelines recommended for reporting animal research

Laboratory animals	This study used female CDl-nude mice, female BALB/c mice and female NOD-SCID mice between the ages of 8-12 weeks. We also used female C57BL/6mice hemizygous for MMTV-PyMT between 3-6 months of age.
Wild animals	This study did not involve wild animals.
Field-collected samples	This study did not involve samples collected from the field.
Ethics oversight	All animals experiments were approved by the University of Toronto Division of Comparative Medicine.

Note that full information on the approval of the study protocol must also be provided in the manuscript.

Human research participants

Policy information about studies involving human research participants

Population characteristics	Tumour biopsies were obtained from the Ontario Tumour Bank. We did not interact or select any human patients. The tumour bank provided tissues as per desired tumour type.
Recruitment	This study did not involve patient recruitment. We obtained samples from Ontario Tumour Bank which collects samples from deceased patients and patients undergoing surgery or biopsy. We requested 3 tumour types from patients who had not undergone treatments with vascular targeting agents. We also requested samples that were isolated and fixed within 30 minutes to ensure good structure preservation. Our final criteria was that we selected samples based on whether blood vessels could be detected in histology images to ensure we were able to analyze the samples. All other aspects were randomized.
Ethics oversight	Tissues were obtained from Ontario Tumour bank and processed with approval from the Ethics Board. The Ethics Approval number is provided in the manuscript.

Note that full information on the approval of the study protocol must also be provided in the manuscript.